Scientific Reports

https://doi.org/10.1038/s41598-026-36921-4

Article in Press

Synthesis and structural insights of tunable NiO_X–MoO_3–MoS_2 nanocomposites with enhanced photocatalytic performance

Received: 7 October 2025

Accepted: 17 January 2026

Published online: 06 March 2026

Cite this article as: Shalom H., Tahover S., Brontvein O. *et al.* Synthesis and structural insights of tunable NiO_X–MoO_3–MoS_2 nanocomposites with enhanced photocatalytic performance. *Sci Rep* (2026). https://doi.org/10.1038/s41598-026-36921-4

Hila Shalom, Shifra Tahover, Olga Brontvein, Iddo Pinkas, Raanan Carmieli & Lena Yadgarov

Article

Synthesis and structural insights of tunable NiO_x–MoO_3–MoS_2 nanocomposites with enhanced photocatalytic performance

*Hila Shalom[1], Shifra Tahover[1'2], Olga Brontvein[3], Iddo Pinkas[3], Raanan Carmieli[3] and Lena Yadgarov[1]**

[1]Department of Chemical Engineering, Ariel University, Israel.
[2]Alpha Program, Future Scientist Center, Ariel University, Ariel, 4076414, Israel.
[3]Department of Chemical Research Support, Weizmann Institute of Science, Israel.
* Corresponding author : Email: lenay@ariel.ac.il.

Abstract:

We report for the synthesis, structural characterization, and photocatalytic activity of NiO_x-MoO_3-MoS_2 nanocomposites (NCs) with different ratios of MoO_3-MoS_2 (labeled as NMOS, N = NiO_x, MO = MoO_3, S = MoS_2). NiO_x nanoparticles (NPs) were synthesized via a sol–gel method and subsequently annealed with different Mo-precursor ratios to form NMOS NCs. Structural analyses (XRD, TEM, XPS, Raman) confirmed a non-stoichiometric NiO_x core, encapsulated by MoO_3-MoS_2 domains. Optical studies showed band gap tuning from 3.53 eV (NiO_x) to 2.92 eV (NMOS-III), enhancing visible-light absorption. Photocatalytic activity, evaluated through methylene blue (MB) degradation, revealed NMOS-I exhibited the highest efficiency due to balanced phase composition and efficient radical generation, with rapid adsorption and degradation in the first 5 minutes, followed by slower equilibrium adsorption. In contrast, excessive Mo-precursor loading in NMOS-III formed a secondary phase (e.g., NiS), leading to recombination losses and reduced efficiency. This work represents the first demonstration of tunable ternary NMOS NCs and elucidates how precise control of phase ratios and heterointerfaces dramatically enhances photocatalytic activity. These findings highlight the role of phase distribution and interfacial chemistry, offering new possibilities for tailoring NMOS NCs for photocatalytic and environmental applications.

Keywords: NiO, nanoparticles, MoO_3, MoS_2, nanocomposites, dye degradation

1. Introduction

In recent years, the demand for advanced nanomaterials with a wide range of applications, including photodegradation [1,2], energy storage, and catalysis [3], has increased. Nanocomposites (NCs) have garnered significant attention for their ability to combine unique properties of individual components, enhancing performance and enabling multifunctional applications.[4,5] Transition metal oxides are promising due to their chemical stability, natural abundance, cost-effectiveness, and relatively simple synthesis routes.[6] They can also serve as efficient photocatalysts due to the suitable band gaps, stability, oxygen vacancies, surface-active sites, and ability to generate reactive oxygen species (ROS) under UV and visible light irradiation.[6,7] Moreover, the photocatalytic efficiency of metal oxides under visible light can be further enhanced through doping engineering.[8,9] Upon excitation, photogenerated electrons reduce oxygen species to form superoxide radicals ($\cdot O_2^-$), while the corresponding holes oxidize water or hydroxide ions to yield hydroxyl radicals ($\cdot OH^-$). These ROS, in turn, drive the degradation of organic pollutants, bacterial disinfection, and water splitting for hydrogen production, positioning metal oxides as important materials for environmental remediation and energy applications.[10–12]

Nickel oxide (NiO) nanoparticles (NPs) are one of the most common metal oxides that have been extensively studied due to their mechanical,[13] electronic,[14] magnetic,[15] optical,[16,17] and p-type conductivity properties. Therefore, NiO NPs have been utilized in a variety of applications,

including gas sensors,[18] fuel cells,[19,20] catalysts,[21,22] battery materials,[23,24] and supercapacitors.[25,26] NiO NPs crystallize in a cubic structure, with their size and defect concentration, such as nickel vacancies and oxygen interstitials, influencing their magnetic[15] and electronic[14] properties. The NiO NPs can be synthesized using a variety of methods, such as hydrothermal synthesis,[27] electrodeposition,[28] the sol-gel method,[29] and thermal decomposition.[30] Despite these benefits, NiO NPs tend to aggregate due to the strong interparticle binding energy,[31] exhibit low electrical conductivity due to their wide band gap (3.5–3.9 eV),[32] and face challenges in defect control during synthesis, leading to inconsistent performance.[33]

To overcome these limitations, NiO is commonly combined with other metal oxides, such as molybdenum trioxide (MoO_3). MoO_3 has a layered structure of double MoO_6 octahedra stacked by van der Waals forces,[34,35] high surface area,[36] remarkable electronic properties,[37,38] and oxidizing characteristics. As an n-type semiconductor, MoO_3 exhibits an indirect band gap of 3.16 eV (with a direct band gap of 2.27 eV) [39,40] and supports stable photogenerated charge carriers at room temperature.[41] Moreover, this material is thermally stable,[42] has very low toxicity,[43] and is highly catalytic, making it suitable for the hydrogen evolution reaction (HER),[44] gas sensor applications,[45,46] energy storage devices,[47] and other functional applications.[48] MoO_3 can be easily synthesized in various forms, including powder,[49] 2D nanosheets,[50] and nanotubes.[51]

Incorporating MoS_2 into NiO-MoO_3 introduces a layered structure of molybdenum atoms between sulfur layers, enhancing electrical conductivity,[52,53] active edge sites,[54] visible-range light absorption,[55] charge separation, and photocatalytic performance. MoS_2, an n-type semiconductor with an indirect band gap of 1.2 eV (direct 1.8 eV),[55] exhibits stable photogenerated excitons at room temperature due to high exciton binding energy (several hundred meV).[56] Moreover, MoS_2 is thermally stable,[57] not toxic,[58,59] and highly catalytically active,[60] making it promising for HER,[61] gas sensor,[62] lithium-ion battery,[63] and other functional applications.[64,65] MoS_2 can be synthesized as powder, 2D nanosheets, or nanotubes.[66]

NiO-MoO_3-MoS_2 NCs (labeled as NMOS, N = NiO_x, MO = MoO_3, S = MoS_2) hold significant potential due to the synergistic interplay between their individual components**.** NiO_x is a stable p-type metal oxide with strong redox activity, but is limited by its wide band gap and low conductivity. [13–17,32,33] while MoO_3 is an n-type semiconductor with a high surface area, a favorable electronic structure, and good catalytic activity for energy-related applications.[34–40,44–48] MoS_2 further contributes high electrical conductivity, strong visible-light absorption, abundant active edge sites, and robust catalytic performance. [52–56,60–65]

Generally, the use of ternary compounds holds great promise for advancing photocatalysis.[67,68] A ternary photocatalytic system, consisting of three hybridized components, significantly outperforms binary or single-component counterparts by providing broader light absorption, more efficient charge separation and transfer through multi-heterojunction interfaces, and a higher density of surface-active sites. These features effectively suppress electron–hole recombination, prolong charge-carrier lifetimes, and enhance the generation of reactive species for pollutant degradation or solar fuel production.[67,68] Moreover, ternary systems often show improved stability and versatility compared to binary or single-component photocatalysts, due to stronger interfacial interactions and tunable band gaps that optimize redox capabilities.

Despite the lack of direct investigations into the full NMOS system, existing studies on NiO-MoO_3 and MoO_3-MoS_2 composites highlight the potential benefits of integrating these materials.[69,70] Integrating NiO_x with MoO_3 and MoS_2 forms multi-heterojunctions that enhance charge separation, broaden the light-harvesting range, and increase the density of active sites, making NMOS NCs

highly attractive for photocatalytic environmental remediation and energy-conversion applications. Several studies of MoO_3-MoS_2 NCs or nanowires achieved through hydrothermal synthesis exhibit enhanced optoelectronic and catalytic properties.[69] Additionally, research on NiO-MoO_3 and nickel molybdate ($NiMoO_4$) synthesized by spin–coating sol–gel techniques, focusing on their physical and electrochemical properties with polymer additives, highlights the growing interest in Ni-Mo-based hybrids.[70]

This study introduces a novel approach by synthesizing NiO NPs via a sol-gel method and subsequently combining with varying molar ratios of $(NH_4)_2MoS_4$ as a Mo precursor to fabricate tunable NMOS NCs. This underexplored strategy enables precise control over phase composition and interfacial engineering. The unique approach of using $(NH_4)_2MoS_4$ as the Mo source enables the preservation of the NiO structure while promoting the simultaneous and controlled formation of both MoO_3 and MoS_2. The NMOS NCs were characterized using X-ray diffraction (XRD) to determine phase and crystalline structure, transmission electron microscopy (TEM) for morphology, composition, and particle size, X-ray photoelectron spectroscopy (XPS) to probe surface elemental composition and chemical states, and Raman spectroscopy confirmed the vibrational modes and structural features of the MoO_3-MoS_2 domains. The optical properties were assessed via UV-Vis spectrophotometry and photoluminescence (PL) measurements. The strength and novelty of this work lie in the systematic correlation between precursor ratio, phase distribution, heterointerfacial chemistry, and photocatalytic performance, enabled by comprehensive multi-technique characterization, and validated through dye degradation experiments. In-depth insights from electron paramagnetic resonance (EPR) spectroscopy, which reveal reactive radical species and the underlying catalytic mechanism, further establish this study as a benchmark for the rational design of ternary transition-metal oxide/sulfide photocatalysts.

2. Results and Discussion

2.1. Synthesis

The first step in the preparation of NMOS NCs is the NiO_x (X=0-1) NPs synthesis. The NiO NPs were synthesized using the sol-gel method, in which nickel(II) nitrate hexahydrate ($Ni(NO_3)_2 6H_2O$) was first dissolved in distilled water (DI water). Subsequently, a sodium hydroxide (NaOH) solution was added dropwise. This resulted in the formation of a light green nickel hydroxide ($Ni(OH)_2$) precipitate, which was subsequently centrifuged, washed three times with DI water, and dried to yield a pale green paste. The chemical reaction is shown in **Reaction 1.**

Reaction 1: $Ni(NO_3)_2 6H_2O + 2NaOH \rightarrow Ni(OH)_2 6H_2O\downarrow + 2NaNO_3$

Upon annealing at 270 °C for 2 hours, the $Ni(OH)_2$ transformed into black non-stoichiometric NiO_x NPs. The chemical reaction involved in the process is shown in **Reaction 2**[71]:

Reaction 2: $Ni(OH)_2 \rightarrow NiO_x + H_2O$

The second step in the synthesis of NiO_x–MoO_3–MoS_2 NCs involves the growth of a MoO_3–MoS_2 layer encasing the NiO_x NPs. Ammonium tetrathiomolybdate ($(NH_4)_2MoS_4$) was employed as the molybdenum precursor (Mo-precursor), enabling the initial ionic interaction with the NiO_x surface and leading to the formation of the NiO_x–MoS_4^{2-} structure. Different molybdite concentrations (referred to as I, II, and III) were added by varying the molar ratios of $(NH_4)_2MoS_4$. The NCs formation process consisted of sonicating the NiO_x NPs in an aqueous solution of $(NH_4)_2MoS_4$ to ensure homogeneous dispersion and promote surface interaction between the Mo–S species and the NiO_x NPs. This was followed by overnight stirring, allowing sufficient time for uniform deposition of MoS_4^{2-} onto the NiO_x surface, as shown in **Reaction 3**. The driving force for the formation of NiO_x–MoS_4^{2-} intermediate is likely the combination of electrostatic interactions and

the mildly acidic environment generated when $(NH_4)_2MoS_4$ is dissolved in DI water. The NiO_x NPs are p-type semiconductors, due to intrinsic defects such as nickel vacancies or extra oxygen,[72] which results in a positive surface character at acidic pH.[73] These electrostatic interactions ensure close contact between the NiO_x NPs and the surrounding MoS_4^{2-} species, which is crucial for their subsequent crystallization during the annealing step.

Reaction 3: $NiO_x + (NH_4)_2MoS_4 \rightarrow NiO_x - MoS_4^{2-} + 2NH_4^+$

The final phase of the NCs was a 15-minute annealing step, which promoted the crystallization of the MoO_3-MoS_2 phase and facilitated the removal of ammonia (NH_3) and sulfur-based residues. First, the NiO_x–MoS_4^{2-} solution was centrifuged to remove the excess salt residues, and the resulting precipitates were vacuum-dried. Subsequently, the dried powders were placed in quartz ampoules and continuously vacuumed to promote the removal of NH_3 and sulfur-based residues. The ampoule was placed in a horizontal two-zone tube furnace with the powder-containing region positioned in the higher-temperature zone at 520 °C (hot zone), and the opposing end at 350 °C (cold zone). This dual-temperature configuration was deliberately chosen based on the known decomposition temperature of $(NH_4)_2MoS_4$.[74] In the higher-temperature zone (520 °C), intermediate species such as amorphous MoS_3 begin to form, while NH_3 and hydrogen sulfide (H_2S) are simultaneously released and evacuated under vacuum (**Reaction 4**).[74] The cooler zone (350 °C) facilitates the directional migration and condensation of these volatile byproducts, ensuring their safe and gradual removal while preventing uncontrolled sulfur release or recombination. Afterwards, the remaining intermediate species, such as MoS_3, are converted into crystalline MoS_2, while further crystallization and restructuring of the NMOS NCs occur (**Reaction 5**). Moreover, the annealing step plays a crucial role in repairing structural defects within the non-stoichiometric NiO_x. It also enhances the NiO_x crystallinity and stability by reducing structural defects such as nickel vacancies and excess oxygen.[75]

Reaction 4: $(NH_4)_2MoS_4 \rightarrow 2NH_3 + H_2S + MoS_3$

Reaction 5: $NiO_x - MoS_4^{-2} + 2NH_4^{+1} \rightarrow NiO_x - MoS_2 + 2NH_3 + H_2S + S$

The 15-minute annealing time was chosen based on several considerations. First, the decomposition of $(NH_4)_2MoS_4$ into the intermediate MoS_3, followed by its conversion into MoS_2 and MoO_3, is known to occur rapidly at 520 °C.[74] Literature studies indicate that these transformations initiate within minutes, making 15 minutes an appropriate and controlled thermal window.[76] Second, under vacuum conditions at high temperatures, prolonged heating can lead to the excessive evaporation of sulfur species (e.g., S_2, H_2S), which may reduce the formation of crystalline MoS_2.[77] Limiting the annealing time helps to minimize sulfur loss while still allowing essential phase transitions. Additionally, prolonged exposure to sulfur residues increases the likelihood of side reactions between sulfur and NiO_x, potentially leading to the formation of undesired nickel sulfide (NiS) phases.[76] A short annealing time helps suppress such secondary reactions, ensuring better phase purity and structural integrity of the final NiO_x–MoO_3–MoS_2 NCs.

The presence of NiO_x within the NMOS NCs during the annealing process at 520 °C may cause additional side reactions to occur during the thermal decomposition of MoS_3 to MoS_2. Although NiO_x does not serve as a direct oxidant, it can release lattice oxygen under high temperature, thereby acting as a catalytic or surface-active species that modifies the local redox environment and facilitates reaction pathways.[78] During the decomposition of MoS_3 under vacuum, sulfur residues are released as a byproduct (**Reaction 6**). Those sulfur residues can react with the NiO_x surface, leading to the partial formation of nickel sulfide (NiS) as a secondary phase and oxygen (O_2) released (**Reaction 7**).

The sol-gel synthesis of NiO_x produces $NaNO_3$ as a byproduct (**Reaction 1)**, which may not be entirely removed during the washing procedure and can persist in the final product. As $NaNO_3$ is

highly water-soluble, completely removing Na^+ and NO_3^- ions can be complex because of their adsorption on the surface of extremely fine $Ni(OH)_2$/NiO fine particles. Therefore, even after three rounds of washing with DI water, some ions may remain adsorbed on the particle surfaces or become trapped within an evolving gel-like network, where $NaNO_3$ can be physically entrapped and shielded from removal.[79] As a result, $NaNO_3$ residues may remain in the dried and calcined NiO_x powder. During the subsequent annealing step in the encapsulation process, this residual $NaNO_3$ can decompose to form reactive oxygen species such as sodium nitrite ($NaNO_2$) and O_2 (**Reaction 8**).[80]

Since all the reactions occur within the same 15-minute annealing window, the O_2 released during this period (**Reaction 7-8**) can effectively oxidize the MoS_3 to MoO_3, particularly under vacuum, where molecular oxygen availability is otherwise limited (**Reaction 9**). The relatively low O_2 content ensures controlled and stepwise oxidation.

Reaction 6: $MoS_3 \rightarrow MoS_2 + \frac{1}{2}S_2\uparrow$

Reaction 7: $\frac{1}{2}S_2 + NiO_x \rightarrow NiS + \frac{1}{2}O_2\uparrow$

Reaction 8: $NaNO_3 \rightarrow NaNO_2 + \frac{1}{2}O_2\uparrow$

Reaction 9: $2MoS_3 + 4O_2 \rightarrow 2MoO_3 + 2SO_2$

2.2. Structural Analysis

The X-ray diffraction (XRD) patterns in **Figure 1** display the structural characteristics of NiO_x and NMOS-I-III NCs. The successful synthesis of NiO_x NPs in the cubic phase (PDS 00-073-0450) is evident from prominent diffraction peaks at 37.2°, 43.3°, 62.8°, 75.4°, and 79.36°, which correlate to the *111*, *200*, *220*, *311*, *and 222* planes, respectively.[81] In addition to the characteristic XRD pattern of NiO, we observe an additional peak at 29.29° that can be assigned to $NaNO_3$, which constitutes ~8% of the total. (PDS 98-000-0333). The presence of $NaNO_3$ is likely a residual byproduct from the sol-gel process utilized in the synthesis of NiO_x NPs (**Reaction 1**).

The XRD pattern for the NMOS-I and NMOS-II NCs (**Figure 1 – red and blue**) shows that the samples contain ~ 96 % NiO, ~3 % MoO_3 (PDS 04-008-4547), and traces of molybdenum disulfide. The oxidation pathway leading to the formation of MoO_3 involves a reaction between MoS_3, formed during the decomposition of $(NH_4)_2MoS_4$, and residual $NaNO_3$ that remains trapped within the gel-like network formed during the sol–gel synthesis of NiO_x. During the annealing process at 520 °C, this residual $NaNO_3$ decomposes to produce reactive oxygen species, such as $NaNO_2$ and O_2, as shown in **Reaction 8**.[80] Indeed, while the NiO_x XRD pattern shows approximately ~8% of $NaNO_3$, it's completely absent in the NCs' patterns, which further supports the proposed transformation pathway. Namely, the decrease in $NaNO_3$ suggests that it was consumed by oxidation reactions, likely through the release of oxygen species that facilitated the oxidation of MoS_3 to MoO_3.

As expected, at low initial concentrations of MoS_4^{2-}, only trace amounts of MoS_2 (PDF 04-026-7897) were detected, partly due to the presence of oxidation-promoting species in the reaction environment. The low molybdate content observed in the XRD patterns can be attributed to several factors. First, the Ni:Mo precursor ratios were relatively low, approximately 4:1 for NMOS-I and 2:1 for NMOS-II, which limited the availability of molybdenum for MoS_2 formation. Second, the oxidation of MoS_3 to MoO_3 during annealing by the byproducts of O_2 and $NaNO_3$. Additionally, the relatively short annealing time (15 min at 520 °C) may be insufficient for the complete conversion of MoS_3 into well-crystallized MoS_2, resulting in the partial formation of amorphous MoS_2 that is undetectable by XRD. Moreover, if only a small percentage of MoS_2 is formed, it will

be challenging to detect by XRD due to its minimal thickness, insufficient mass, and weak diffraction intensity.[82] Indeed, the characteristic (002) reflection, which indicates the layered structure, is often very weak or completely absent in monolayer and few-layer samples.[83] In addition, turbostratic disorder and poor crystallinity further reduce XRD visibility. As a result, XRD cannot reliably confirm the presence of MoS_2; this reflection becomes discernible only as the number of layers increases and crystallinity improves.

The XRD pattern for the NMOS-III sample (**Figure 1 – green**) reveals a more complex composition: 56.8% NiO, 25.3% MoO_3, 9.6% NiS (PDS 98-000-0308), and 8.3% MoS_2. NiS forms due to a reaction between the NiO and the sulfur in MoS_2 (**Reaction 6-7**Reaction 7). These results indicate that increasing MoS_4^{2-} concentration makes the formation of various Mo-based oxides and NiS more pronounced, suggesting complex interactions between NiO_x and MoS_4^{2-} at the interface.

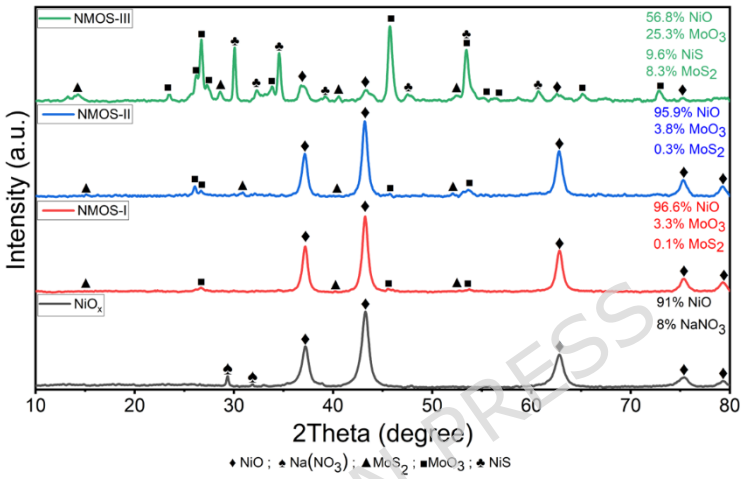

Figure 1: XRD patterns of NiO_x NPs (black) and NMOS NCs prepared with varied precursor ratios: NMOS-I (red), NMOS-II (blue), and NMOS-III (green). The diffraction peaks are indexed to ♦ NiO (PDF 00-073-0450), ♠ $NaNO_3$ (PDF 98-000-0333), ■ MoO_3 (PDF 04-008-4547), ▲ MoS_2 (PDF 04-026-7897), and ♣ NiS (PDF 98-000-0308).

The synthesis of non-stoichiometric NiO_x NPs resulted in oval-shaped NPs with an average diameter of approximately 8±3 nm (**Figure 2A-B**). **Figure 2A** displays a representative TEM image of the NPs, while **Figure 2B** shows the corresponding size distribution. A representative HR-TEM image of a single NiO_x NP is shown in **Figure 2A - insert**. The image reveals well-defined lattice fringes with an interplanar spacing of 0.241 nm, corresponding to the (*111*) plane of cubic-phase NiO.[81] The crystallinity of the NPs was further confirmed by the Selected Area Electron Diffraction (SAED) pattern shown in **Figure 2C**, which displays distinct concentric diffraction rings. These rings can be indexed to the (*111*), (*200*), (*220*), and (*311*) planes, confirming the face-centered cubic structure of NiO.[81] The EDS analysis (**Table 1**and **Figure S1**) revealed that the NiO_x NPs contain ~57 at% Ni and ~43 at% O, corresponding to a Ni:O atomic ratio of 1:0.75. This deviation from the ideal stoichiometry of NiO (1:1) suggests the presence of nickel-rich phases or oxygen vacancies.[75]

Table 1: Results of the semi-quantitative EDS analysis from TEM images

	Nickel (Ni) (at%)	Oxygen (O) (at%)	Molybdenum (Mo) (at%)	Sulfur (S) (at%)	Ni: O
NiO_x	57.3 ± 3.6	42.7 ± 3.6			1: 0.75
NMOS-I	56.8 ± 3.6	43.2 ± 3.4			1:0.76
	25.7 ± 3.5	59.0 ± 4.8	11.1 ± 4.0	4.2 ± 2.7	
NMOS-II	22.0 ± 2.6	58.6 ± 3.1	13.5 ± 2.3	5.9 ± 2.9	

NMOS-III	13.8 ± 3.4	52.2 ± 3.2	18.2 ± 3.4	15.7 ± 3.6

During the synthesis of NMOS NCs, the NiO_x NPs underwent an additional 15-minute annealing step at 520 °C to crystallize the MoO_3-MoS_2. This temperature is significantly higher compared to the formation temperature of the NiO_x NPs (270 °C). The elevated thermal treatment not only facilitated the crystallization of the MoO_3-MoS_2 mixture but also induced further growth and enhanced crystallinity within the NiO_x NPs.[75,84] Consequently, the annealed NiO_x NPs exhibited an increased average particle size of approximately 13 ± 4 nm, as shown in **Figure 2D-E**. Clear lattice fringes are observed with an interplanar spacing of 0.241 nm, corresponding to the (*111*) plane of cubic-phase NiO, confirming the improved crystallinity following the high-temperature annealing (**Figure 2D** – insert).[81] In **Figure 2F,** the SAED pattern shows distinct concentric diffraction rings of the FCC structure of NiO.[81] EDS measurements (**Table 1**) revealed that the non-stoichiometric NiO_x NPs contain 57 at% Ni and 43 at% O, corresponding to a Ni:O atomic ratio of 1:0.76.

HR-STEM analyses of the NMOS NCs (**Figure 2G-L**) reveal well-defined NiO_x NPs embedded within molybdate-derived structures. Orthorhombic MoO_3 crystallites are distinguished by lattice fringes with an interplanar spacing of 0.366 nm corresponding to the (001) plane. The NiO_x NPs display lattice fringes with a spacing of 0.241 nm, assigned to the (111) plane of cubic NiO.[81] In all cases, EDS elemental mapping (**Figure 2G-H**, **J-K**, **M-N**) demonstrates the presence of Ni, O, Mo, and S, and the semi-quantitative analysis (**Table 1**) confirms their presence in agreement with the designed composite structure.

The differences among the samples with varying amounts of molybdate precursor are manifested in changes to MoO_3 NP size, composition, and crystallinity, each of which is directly correlated with the precursor concentration. In the NMOS-I sample (**Figure 2I**), MoO_3 crystallites are relatively small (~5–7 nm) and display the (011) plane with a spacing of 0.255 nm. In the NMOS-II sample (**Figure 2L**), MoO_3 NPs grow to ~21 nm, reflecting the effect of increased $(NH_4)_2MoS_4$ loading in promoting the development of larger domains. In the NMOS-III sample (**Figure 2O**), the MoO_3 NP size further increases to ~33 nm, demonstrating that precursor concentration strongly drives nucleation and coarsening of MoO_3 crystallites. The compositional trends follow the same pattern: the NMOS-I NCs contains 25.7% Ni, 59.0% O, 11.1% Mo, and 4.2% S, the NMOS-II NCs shows increased Mo and S (13.5% Mo, 5.9% S) with reduced Ni (22.0%), while the NMOS-III NCs exhibits the most pronounced enrichment in Mo (18.2%) and S (15.7%) alongside a decrease in Ni (13.8%) and O (52.2%). These differences are consistent with XRD analysis (**Figure 1**), where MoO_3 reflections intensify and sharpen from the NMOS-I to NMOS-III samples, confirming the enhanced crystallinity and higher fraction of the MoO_3 phase at increasing precursor concentrations.

Article

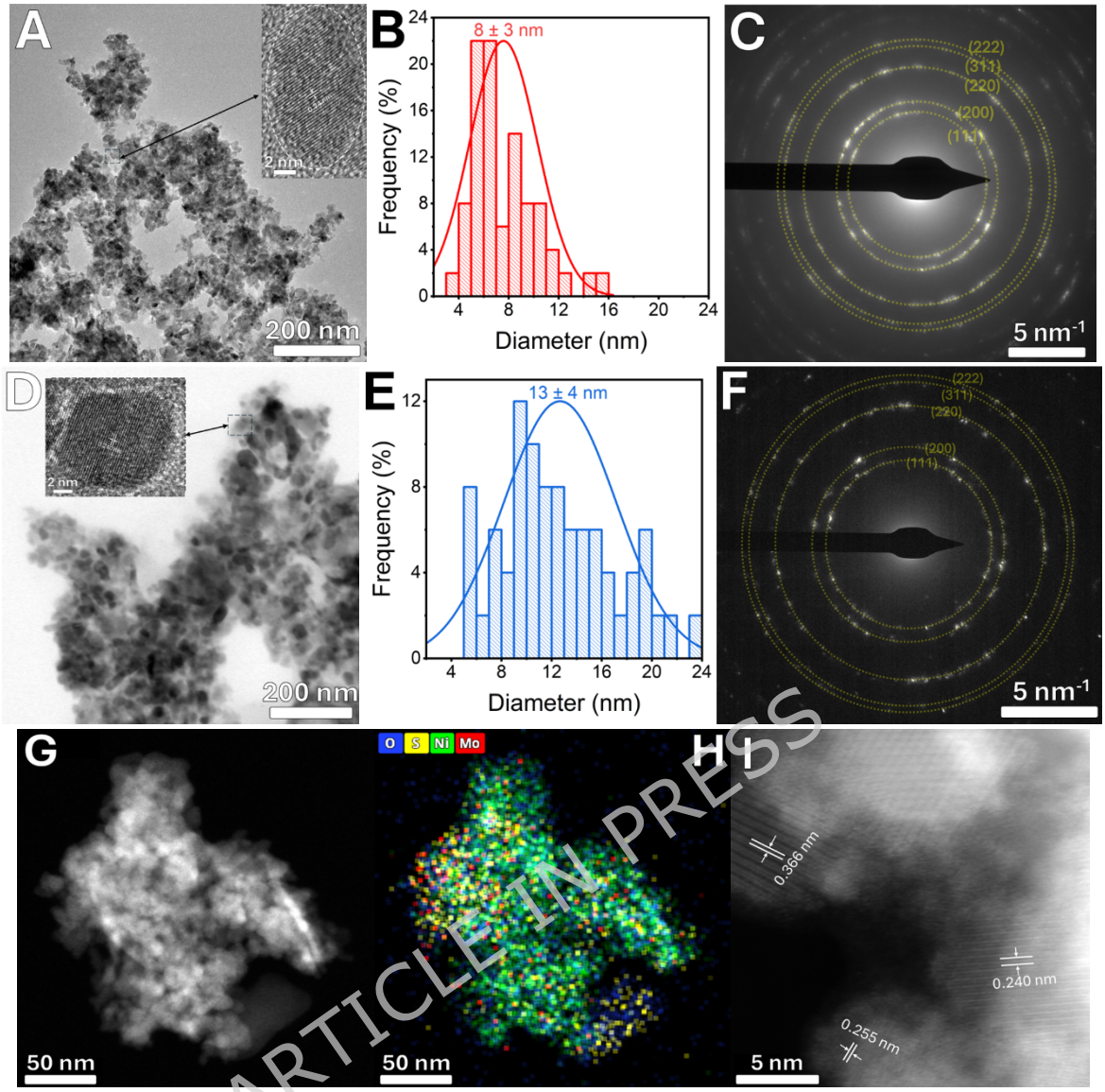

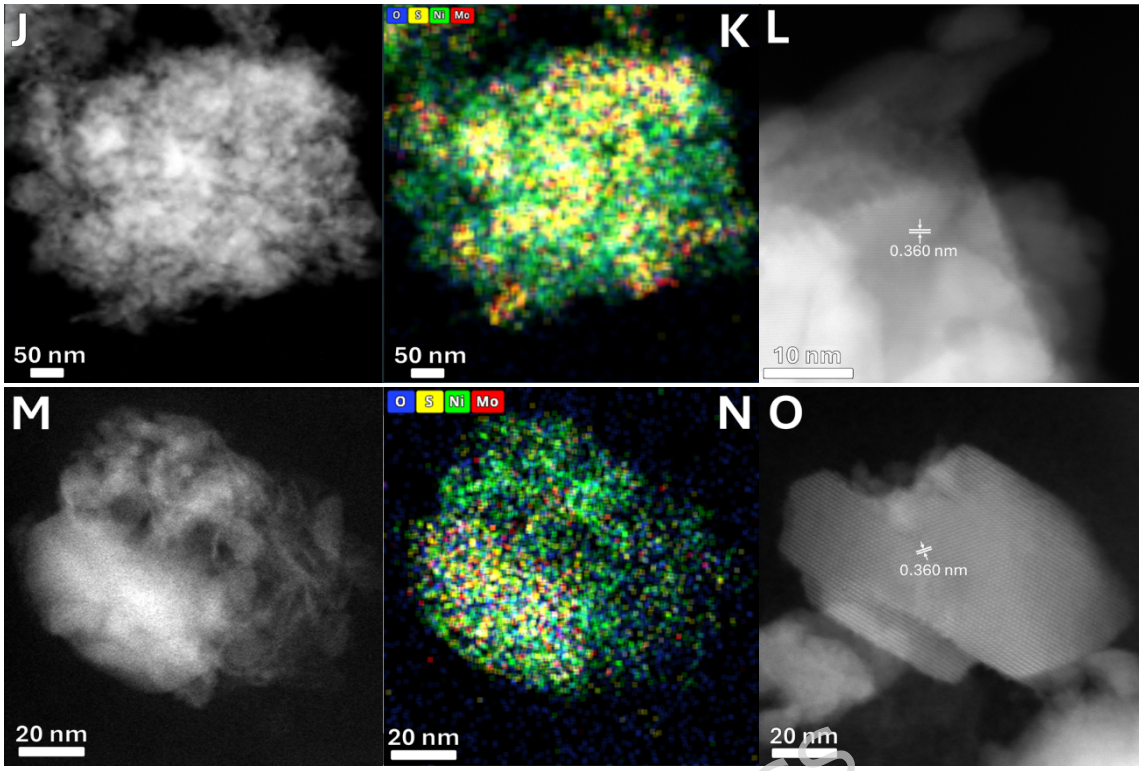

Figure 2: HR-TEM images and related analyses of NiO_x NPs and NMOS-I-III NCs are presented as follows: (A) NiO_x NPs, with an inset showing a high-resolution image of a single NP; (B) Size distribution histogram of NiO_x NPs; (C) SAED pattern of NiO_x NPs; (D) annealed NiO_x NPs, with an inset showing a high-resolution image of a single NP; (E) Size distribution histogram of annealed NiO_x NPs; (F) SAED pattern of annealed NiO_x NPs; (G, J, M) HR-TEM images of NMOS-I-III NCs displaying particle morphology; (H, K, N) corresponding EDS mapping for NMOS-I-III NCs; and (I, L, O) images of the lattice fringes for NMOS-I-III NCs, respectively.

The X-ray photoelectron spectroscopy (XPS) spectra of NiO_x and NMOS-I-III NCs are shown in **Figure 3A-K**, providing insight into their electronic structure, chemical composition, and surface states. Depth profiling was performed on the NCs to obtain representative information from both the NiO_x NPs and their interface with the MoO_3–MoS_2 domains.

For NiO_x NPs (**Figure 3A-B**), the Ni 2p and O 1s peaks are clearly observed. Background subtraction was performed using the Shirley method. The O 1s spectrum, deconvoluted with Shirley background subtraction, shows two main components: a peak at 530.03 eV corresponding to lattice oxygen (M–O) in NiO, and a higher binding energy peak at 532.09 eV associated with surface hydroxyl groups or adsorbed species (C–O/Ni–OH). Notably, nickel species are progressively reduced during XPS depth profiling with Al Kα radiation, revealing lower oxidation states and even the presence of metallic Ni. The Ni 2p spectrum displays a complex envelope arising from multiple oxidation states and satellite features. The main Ni^{2+} peaks appear at 855.01 eV ($2p_{3/2}$) and 872.40 eV ($2p_{1/2}$), with shake-up satellites at 860.78 eV and 879.91 eV, characteristic of Ni^{2+} in NiO. Peaks at 857.07 eV ($2p_{3/2}$) and 873.82 eV ($2p_{1/2}$), with additional shake-up at 864.00 eV and 883.50 eV, indicate Ni^{3+} species with minor Ni^{+} contributions appear at 853.70 eV and 870.78 eV. These multiple valence states confirm the non-stoichiometric nature of NiO_x, consistent with oxygen vacancies or partial surface reduction/oxidation. TEM–EDS analysis further supports this interpretation, showing a Ni:O atomic ratio of ~1:0.75. XPS quantification yields Ni and O atomic percentages of 62.5% and 37.5%, respectively (**Table S1**), confirming the nickel-rich composition of the material.

In the NMOS-I NCs (**Figure 3C-E**), the Ni 2p and O 1s peaks remain at similar binding energies but with reduced intensities (54.8% Ni and 37.8% O). This reduction reflects surface modification caused by Mo incorporation. In the Mo 3d region, the peaks at 232.7 eV and 235.6 eV correspond to Mo^{6+} (Mo $3d_{5/2}$ and $3d_{3/2}$), indicative of MoO_3 or related oxides. Additional peaks at 228.6 eV and 230.6 eV are characteristic of Mo^{4+} in MoS_2, while the small peak at 225.9 eV corresponds to the S 2s signal. These results confirm the coexistence of MoO_3 and MoS_2 phases, with partial oxidation of MoS_2 likely occurring during annealing or through interactions with NiO_x. The quantified contributions from Mo^{6+}, Mo^{4+}, and S 2s are 4.5%, 2.2%, and 0.7%, respectively.

Increasing the Mo-precursor to NMOS-II NCs changes the relative intensities of the peaks without shifting their binding energies (**Figure 3F-H**). XPS quantification reveals atomic percentages of 59.7% Ni, 31.7% O, 4.3% Mo^{6+}, 3.3% Mo^{4+}, and 1.0% S. These results confirm that NiO_x remains the dominant phase, but the sample is increasingly enriched in the composite with Mo^{4+}/Mo^{6+} species and sulfur, yielding a mixed MoO_3–MoS_2 composition. The partial oxidation of MoS_2 is consistent with annealing-induced oxidation processes.

For the NMOS-III NCs (**Figure 3I-K**), the Ni, O, Mo, and S signals undergo further redistribution. The atomic percentages are 43.4% Ni, 28.9% O, 7.9% Mo^{6+}, 13.4% Mo^{4+}, and 6.4% S. The higher S 2s intensity compared to the NMOS-I and NMOS-II samples suggests increased incorporation of MoS_2, along with the possible formation of NiS as a secondary phase due to chemical interactions between NiO_x and the MoS_4^{2-} precursor. The simultaneous presence of NiO_x, MoO_3, and MoS_2 phases, along with traces of NiS, underscores the complex chemical interplay that occurs during precursor decomposition and annealing.

In summary, XPS analysis reveals that increasing the Mo-precursor concentration results in higher Mo and S content, indicating the formation of larger MoO_3 and MoS_2. The NiO_x phase remains dominant but undergoes surface modification, with evidence of partial MoS_2 oxidation and possible NiS formation at higher concentrations. These findings confirm the tunable composition and complex interfacial chemistry of the nanocomposites.

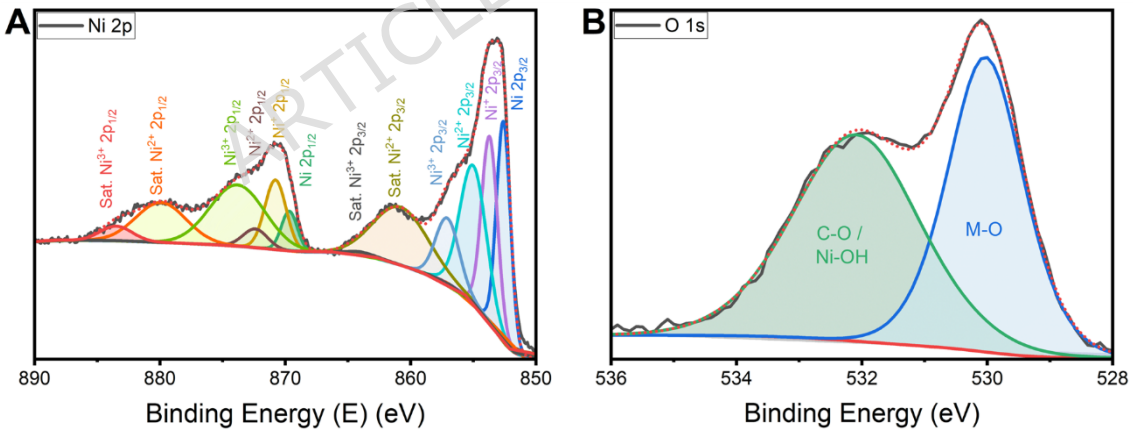

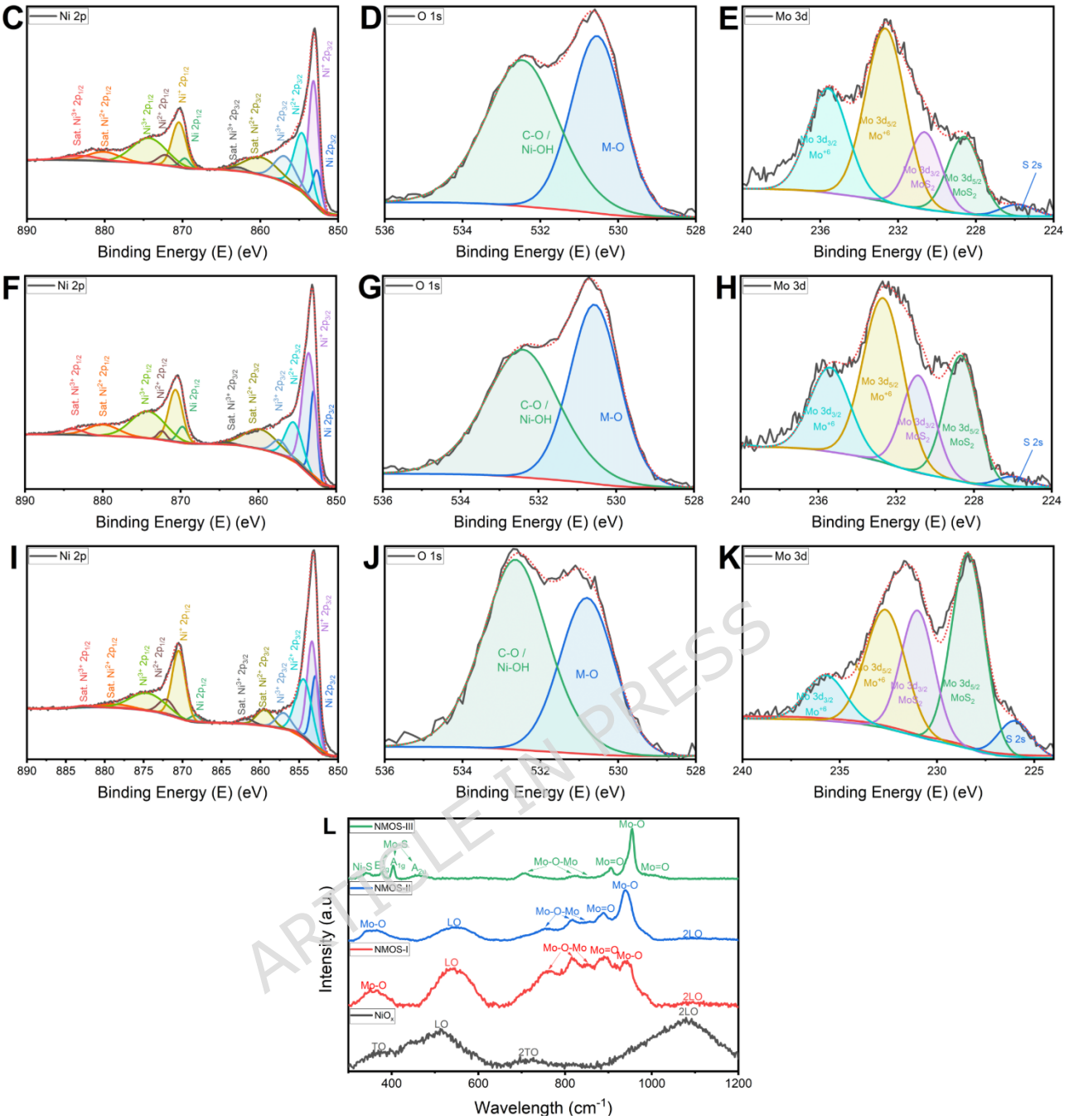

Figure 3: XPS spectra of NiO_x and NiO_x–MoO_3–MoS_2 NMOS): (A) Ni 2p and (B) O 1s for NiO_x; (C) Ni 2p, (D) O 1s and (E) Mo 3d for NMOS-I; (F) Ni 2p, (G) O 1s and (H) Mo 3d for NMOS-II; (I) Ni 2p, (J) O 1s and (K) Mo 3d for NMOS-III. (L) Raman spectra of NiO_x NPs (black) and NMPS NCs prepared with different Mo-precursor ratios: NMOS-I (red), NMOS-II (blue), and NMOS-III (green).

2.3. Spectroscopic Analysis

Raman spectra of NiO_x and NMOS-I-III NCs are shown in **Figure 3L**, providing characteristic vibrational signatures, structural features, and phase composition. The corresponding peak assignments are summarized in **Table S2**. Across all samples, NiO-related modes are detected, though their intensity and visibility decrease progressively with increasing precursor concentration. At the same time, MoO_3-related peaks are consistently observed in the composites, and their number, position, and intensity evolve with Mo precursor loading. These observations confirm the coexistence of NiO_x and Mo-derived phases, with variations in spectral features reflecting changes in nanoparticle size, structural integration, and phase composition.

The differences between the samples are evident in both the identity and relative intensities of the Raman bands. The spectrum of pristine NiO_x (**Figure 3L - black**) is dominated by Ni–O vibrations, with sharp features at ~514 and ~1077 cm^{-1} corresponding to the first-order longitudinal optical (LO) and second-order longitudinal optical (2LO) modes, respectively, and additional peaks at ~398 and ~725 cm^{-1} assigned to first-order transverse optical (TO) and second-order transverse optical (2TO) modes.[85,86] The sharp peak at 514 cm^{-1} is particularly significant, as it is commonly associated with Ni-related defects,[86] reflecting the non-stoichiometric nature of the synthesized NiO_x.

In the NMOS-I sample (**Figure 3L - red**), the NiO signals decrease in intensity and shift slightly (~538 and ~1093 cm^{-1}), which can be explained by the growth of larger NiO NPs during annealing,[87] as confirmed by TEM. At the same time, six new bands emerge that are characteristic of MoO_3: ~356 cm^{-1} (Mo–O bending), ~765 cm^{-1} (O–Mo–O bridge stretching), ~819 and ~851 cm^{-1} (Mo–O–Mo symmetric stretching), ~891 cm^{-1} (terminal Mo=O stretching), and ~940 cm^{-1} (polyoxometalate-type Mo–O stretching).[88,89] These features confirm the coexistence of NiO and MoO_3, in agreement with XRD and XPS results.

In the NMOS-II spectrum (**Figure 3L - blue**), the NiO contribution is further reduced, with only a weak LO mode at ~545 cm^{-1} detected. In contrast, MoO_3-related signals intensify, including peaks at ~364 cm^{-1} (Mo–O bending), ~756–763 cm^{-1} (Mo–O–Mo stretching), ~816 cm^{-1} (Mo=O stretching), ~858 and ~888 cm^{-1} (Mo–O stretching and bending), and ~940 cm^{-1} (polyoxometalate-type stretching). These results show that higher precursor loading enhances the vibrational contributions of MoO_3 while masking most NiO modes, consistent with the structural integration suggested by XRD and XPS.

Finally, in the NMOS-III sample (**Figure 3L - green**), the NiO-related modes disappear entirely, indicating their suppression by Mo-rich and sulfide phases. Strong MoO_3 vibrations are observed at ~707, 824, 863, 905, 953, and 1007 cm^{-1}, several of which are shifted to lower wavenumbers due to lattice softening caused by the growth of larger MoO_3 NPs (~33 nm, TEM). In addition, MoS_2 fingerprints are clearly detected at ~376 cm^{-1} (E^1_2g), ~403 cm^{-1} (A_1g), and ~460 cm^{-1} (A_1u), consistent with the increased MoS_2 fraction at this loading.[90] A low-frequency band at ~344 cm^{-1} is also present, assigned to NiS vibrations,[91] confirming partial sulfide formation via interaction between NiO_x and the MoS_4^{2-} precursor during annealing. Together, these observations highlight the progressive transition from NiO-dominated spectra to MoO_3- and MoS_2-rich vibrational signatures, with additional NiS contributions at the highest precursor concentration.

The absorption spectra of NiO_x and NMOS-I-III NCs are displayed in **Figure 4A**. All the spectra exhibit absorption in the UV–visible region, with an absorption edge around 300 nm corresponding to the presence of NiO_x NPs.[92,93] As the Mo content increases, the spectra show apparent broadening and splitting of the absorption band, indicating changes in the electronic structure. Deconvolution of the absorbance spectra (**Figure 4B-E**) enables a more detailed interpretation of these features, allowing for tracing the individual spectral contributions of MoO_3 and MoS_2.

The NiO_x NPs deconvolution (**Figure 4B**) reveals three distinct peaks at 248, 298, and 300 nm. The peaks in 248 and 298 nm are characteristic of NiO_x NPs with an average size of ~8 nm.[92–94] The third broad peak at 300 nm is typical of $NaNO_3$ and corresponds to the weak $n \rightarrow \pi^*$ electronic transition within the nitrate ion.[95] The presence of $NaNO_3$, a byproduct of the sol–gel synthesis of NiO_x, is further supported by XRD analysis.

The absorbance spectrum of NMOS-I NCs displays more pronounced and sharper peaks at 262 nm and 303 nm (**Figure 4C**). Moreover, the first one appears to be more intense with reduced FWHM. The 262 nm peak, associated with NiO_x, exhibits a red shift compared to pristine NiO_x, likely due to increased particle size (~13 ± 4 nm, confirmed by TEM) and reduced quantum confinement

effects (**Figure 2B**, **E**). In addition, the shift and narrowing of the NiOx peak can also be ascribed to the annealing process, as well as the formation of additional Mo-related phases. Namely, the electronic interactions between NiO_x and MoO_3–MoS_2 modify the transition energies. Indeed, the absorbance peak at 303 is most likely attributed to the presence of MoO_3,[96] which forms during the annealing process with the Mo-precursor (**Reaction 9**). That ascription is further supported by the comparatively higher dielectric function of MoO_3, which enhances its optical response in this region, resulting in a more intense and distinct absorbance peak.[97,98] Spectrum deconvolution supporting this interpretation (**Figure 4C**), as it resolves additional broad spectral contribution at 310 nm, which is assigned to the defects within the NCs as well as MoO_3.[99]

As the concentration of the Mo-precursor increases to NMOS-II NCs, the characteristic NiO_x-related absorption features diminish markedly, with the NiO_x peak nearly disappearing from the spectrum. Instead, the absorption is dominated by an edge around 300 nm, corresponding to MoO_3. This shift occurs as the NiO_x is embedded within a MoO_3–MoS_2 matrix, which suppresses its optical response. The latter observation is supported by TEM, XRD, and Raman analysis, showing increased MoO_3 and reduced NiO_x signals. Similar to the NMOS-I NCs, spectral deconvolution of the NMOS-II absorption profile (**Figure 4D**) resolves three peaks at 262, 303, and 315 nm, with the latter two attributed to MoO_3. As observed in TEM, the red shift of the third peak from 310 nm to 315 nm suggests further MoO_3 growth and dielectric enhancement, consistent with larger MoO_3 domains.

For the NMOS-III sample, the absorption spectrum exhibits extended absorption into the visible region (400–800 nm), which is a result of the higher concentration of MoS_2.[100] The absorption's deconvolution presents a complex mixture of multiple peaks at 262, 272, 305, and 728 nm (**Figure 4E**). The band at 262 nm is associated with NiO_x, and the decrease in its full width at half maximum (FWHM) indicates changes in its local electronic environment within the Mo-rich matrix. The peak at 272 nm corresponds to NiS,[101] formed through interaction of NiO_x with the Mo-precursor during annealing, while the 305 nm band is attributed to MoO_3, and is consistent with its stronger crystallinity and dielectric response.[96,99,102] The broad peak at 728 nm arises from overlapping contributions of MoS_2 and Mo-based sub-oxides. These results confirm the multiphase nature of the NMOS-III nanocomposite, consistent with the phase distribution observed in Raman, XRD, and XPS analyses.

To summarize, NiO_x and NMOS-I-II NCs samples exhibit a clear absorption edge in the UV region, dominated by NiO_x and MoO_3 contributions, with negligible absorption above 400 nm. By contrast, NMOS-III exhibits extended visible-light absorption due to MoS_2 and secondary Mo phases, reflecting its multiphase character.

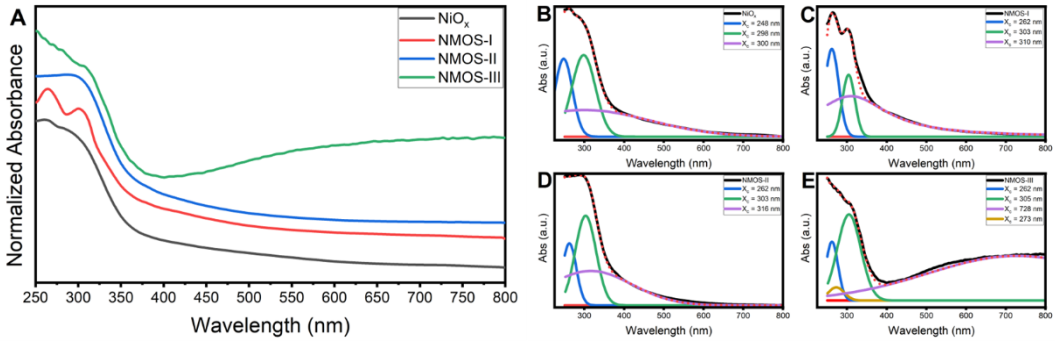

Figure 4: (A) Absorption spectra of NiO_x NPs and NMOS-I-III NCs with various Mo-precursor ratios; (B–E) spectral deconvolution of NiO_x and NMOS-I-III NCs.

The band gap values of NiO and NMOS-I-III NCs are shown in **Figure S2**. Pure NiO_x NPs exhibit a band gap of 3.53 eV, consistent with reported values.[103] Upon introducing the Mo-precursor, the band gap increases to 3.66 eV in the NMOS-I sample. This shift can be attributed to the growth

and improved crystallinity of NiO_x during annealing, together with the formation of MoO_3 domains. As the NiO_x is most likely embedded within the MoO_3–MoS_2 matrix, this results in a modified electronic structure and a slight blue shift of the absorption edge. Interestingly, at a 2x Mo-precursor concentration, the band gap of NMOS-II NCs red shifts back to 3.53 eV. This red shift is attributed to the growth of separated MoO_3 domains, which increase the NiO-MoO_3 phase segregation and separation. This interpretation is further supported by XRD, which reveals intensified MoO_3 reflections, Raman spectra show suppression of NiO_x vibrational modes by Mo-rich phases, and XPS data confirm increased Mo^{6+}/Mo^{4+} contributions. In contrast, for NMOS-III, the band gap shifts to 2.93 eV. The profound shift can be attributed to the formation of MoS_2 and NiS. The presence of MoS_2 introduces broad band-edge transitions, extending optical absorption into the visible range.

The emission spectra of NiO_x and NMOS-I-III NCs at an excitation wavelength (λ_{ex}) of 250 nm and 532 nm are shown in **Figure 5A-B**, respectively. The 250 nm excitation is for the NiO_x component, while the 532 nm excitation is selective for the Mo-component.

Under excitation at 250 nm, the PL spectra of all samples display the same emission profile with varying intensities (**Figure 5A**). Deconvolution reveals three prominent peaks at 380, 497, and 601 nm, together with a broad band at 463 nm (**Figure S3**). Since the spectral shape remains essentially unchanged across all samples, only the NiO_x deconvolution is shown in **Figure S3**, while the fitting parameters for the composites are summarized in **Table S3**. The emission at 380 nm represents near-band-edge (NBE) transitions typical in wide-band gap semiconductors like NiO_x. This strong peak is ascribed to excitonic recombination between the conduction and valence bands within the band edge.[104] The board 463 nm peak and 497 nm peak are associated with structural defects such as oxygen vacancies and interstitials in NiO_x.[105] Whereas the 601 nm band is attributed to transitions from the conduction band to the *d*-band within NiO_x's band structure, aligning with its estimated Fermi level energy.[106] For NMOS-I, the emission intensity is nearly doubled compared to pristine NiO_x, probably due to energy transfer from MoO_3 defect states, as supported by XRD, TEM, XPS, and Raman analyses. In contrast, the emission of NMOS-II NCs is only slightly enhanced compared to the NiO_x. This enhancement is attributed to MoS_2 contributions, which extend absorption but also introduce non-radiative pathways that partially suppress emission.[107] NMOS-III exhibits significantly reduced PL compared to the NiO_x, which can be attributed to the presence of a multiphase composition (NiO, NiS, MoO_3, and MoS_2), as confirmed by the other results. This complex phase mixture introduces non-radiative recombination centers and contending energy transfer pathways that quench emission. Namely, the lower PL intensity likely arises from defect states and electronic transitions specific to the NiS and MoS_2 phases, which differ from pure NiO_x transitions and contribute weaker overall emissions.

When excited at 532 nm, the emission is much lower in intensity due to the low Mo-content (**Figure 5B-F** and **Table S4**). The pristine NiO_x exhibits weak emission with a broad background and a shoulder-like peak at 633 and 661 nm (**Figure 5C** and **Table S4**). The background is attributed to deep-level defects, particularly oxygen vacancies, while the shoulder features originate from defect-related states associated with the non-stoichiometric NiO_x lattice.[105] In NMOS-I NCs, the emission intensity increased, and the broad background is blue-shifted. The 633 nm peak becomes more distinct, and the 661 nm shoulder-like feature broadens and strengthens. These enhancements are attributed to the presence of Mo-based additives (**Figure 5D**).

In NMOS-II NCs, the broad background is red-shifted with additional peaks at 629, 670, and 723 nm (**Figure 5E**). The 629 nm feature corresponds to the MoS_2 B exciton with a blue shift due to defect-induced lattice distortions. The 670 nm peak is attributed to the MoS_2 A exciton, arising from direct electron–hole recombination in MoS_2,[108,109] and its red shift indicates a subtle increase in MoS_2 layer thickness. The 723 nm band is likely related to defect-bound excitons,

which become more pronounced in few-layer and defect-rich Mo-S phases. In NMOS-III NCs, the overall emission is reduced compared to NMOS-I NCs and NMOS-II NCs (**Figure 5B**, **F**), reflecting the complex multiphase composition (NiO, NiS, MoO_3, MoS_2) as confirmed by XRD, TEM, XPS, and Raman analyses. Deconvolution reveals a blue-shifted background with additional peaks at 633 and 670 nm, corresponding to MoS_2 B and A excitons, respectively.[108,109] The slight shifts of these excitonic peaks also suggest enhanced defect–exciton interactions, where defects act as trapping or recombination sites that perturb excitonic transitions.

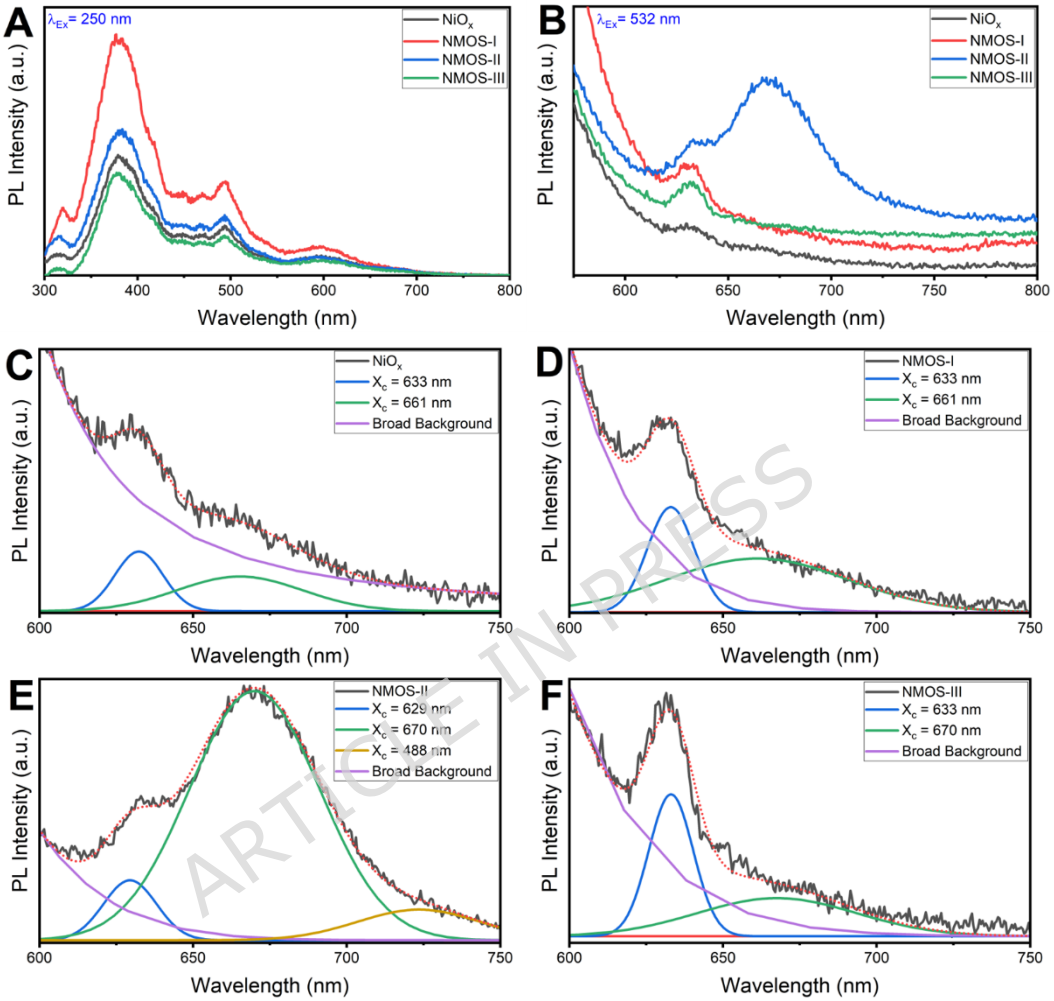

Figure 5: Emission spectra of NiO NPs, NMOS-I, NMOS-II, and NMOS-III NCs measured at excitation wavelengths of 250 nm (A) and 532 nm (B). Deconvoluted PL spectra of (C) NiO_x and (D-F) NMOS-I-III NCs at an excitation wavelength of 532 nm.

2.4. Photocatalysis Analysis

Our findings demonstrate that NMOS NCs exhibit exceptional potential as a photocatalytic system. The unique architecture integrates p-type NiO_x NPs, known for their high theoretical capacitance, with n-type MoO_3-MoS_2 phases. This combination forms efficient p–n junctions at their interfaces, facilitating enhanced charge separation and transfer. Additionally, the combined effect of these phases is expected to improve electronic conductivity and chemical stability, thereby creating an optimal platform for visible-light-driven photocatalysis. These properties position the nanocomposites as a highly promising material for photocatalytic applications.

To elucidate whether Mo-based structures enhance the radical-mediated photocatalytic activity of the NCs, we employed electron paramagnetic resonance (EPR) spectroscopy. This technique

enables the detection and identification of radicals generated in the presence of NCs through the use of spin-trapping agents such as 5-tert-butoxycarbonyl-5-methyl-1-pyrroline N-oxide (BMPO), a nitrone-based spin trap effective for both hydroxyl ($\cdot OH^-$) and superoxide ($\cdot O_2^-$) radicals.[110] To evaluate the formation of the reactive radicals in NiO_x and NMOS-I-III NCs, EPR measurements were conducted in the dark and under visible-light illumination (**Figure S4** and **Figure 6A**).

For both NiO_x and NMOS-III NCs, no EPR signals were observed under dark conditions or visible light irradiation (**Figure S4** and **Figure 6A**), suggesting that no stable radicals were generated. This behavior can be explained by their optical properties: NiO_x NPs have a wide band gap of approximately 3.53 eV, allowing them to absorb light primarily in the ultraviolet rather than visible range. Similarly, NMOS-III NPs NCs contain a high fraction of MoO_3, and also predominantly absorb ultraviolet light. As a result, both NiO_x and NMOS-III exhibit limited photoactivity under visible light, consistent with their relatively poor photocatalytic performance in dye degradation experiments, as will be shown below.

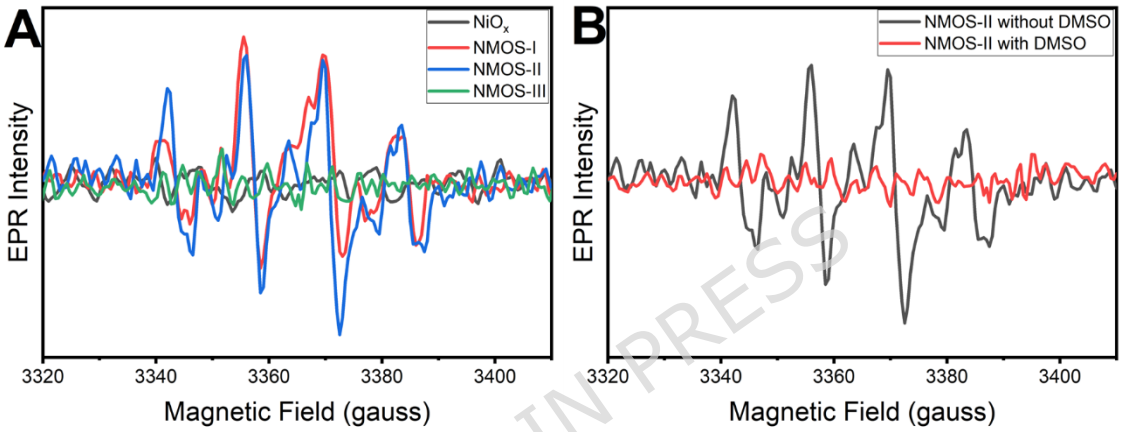

Figure 6: EPR spectra acquired under visible-light illumination of (A) NiO_x and NMOS-I-III with BMPO as a "spin-trap" and (B) NMOS-II NCs under light illumination with and without the addition of DMSO.

For NMOS-I-II NCs, no signals were observed under dark conditions. However, after exposure to visible light, the EPR spectrum exhibits a distinct pattern centered around g = 2, with four lines indicative of interactions with $\cdot OH^-$radicals.[111] Notably, the radical signal intensity of NMOS-II exhibits the strongest response under illumination (**Figure 6A**). Notably, using BMPO as a spin trapping agent in EPR spectroscopy effectively detects reactive oxygen species (ROS) such as $\cdot OH^-$ and $\cdot OOH$ ($\cdot O_2^-$) despite their short half-lives.[112] To establish the formation of $\cdot OH^-$ radicals, the experiments were repeated in the presence of 10% dimethyl sulfoxide (DMSO), which acts as a scavenger for $\cdot OH^-$ radicals, thereby allowing for the distinction between signals induced by different oxygen species.[113][114] The presence of DMSO resulted in a quenched EPR signal for NMOS-II compared to samples without DMSO (see **Figure 6B**). The latter result indicates that the main active radical species formed under illumination of the NMOS-I and NMOS-II is the $\cdot OH^-$. This specific species is the most favorable for advancing oxidation processes, especially in applications such as pollutant and wastewater treatment, soil remediation, and sterilization.[115]

To evaluate the photocatalytic efficacy of NCs, we examined the ability of NiO_x and NMOS-I-III NCs to degrade the methylene blue (MB) dye under visible-light irradiation. MB is an aromatic heterocyclic cationic dye[116] and is considered as one of the most popular clothing colorants in the textile industry [117], known for its environmental persistence and toxicity. Effective degradation of MB demonstrates the NCs' ability to break down complex organic pollutants, highlighting their potential for environmental remediation applications, such as wastewater treatment, by leveraging visible-light-driven photocatalysis to address industrial dye pollution.

Figure 7A shows the change in the absorbance of the MB dye at different time intervals for all the examined catalysts (NiO_x and NCs) in aqueous solutions. The reduction of the MB characteristic absorption maxima (λ_{max} ~665 nm) was used to track the progression of dye degradation. In addition, we assessed the photocatalytic efficiency of all NPs and NCs by comparing the degradation rate (D%), and the kinetics of the photocatalytic reactions, as detailed in the methods section (**Figure S5A**). Following 90 minutes of illumination, the degradation rates of MB dye are as follows: 35% with NiO NPs, 82% with NMOS-I, 73% with NMOS-II, and 42% with NMOS-III (**Figure S5A**). NMOS-I and NMOS-II NCs demonstrated the highest photocatalytic efficiency compared to NiO_x and NMOS-III NCs. The superior performance of NMOS-I can be attributed to the optimal balance between NiO_x and Mo-related phases (1:0.02, as confirmed by XRD). This combination facilitates efficient charge separation and suppresses electron–hole recombination. In contrast, excessive Mo- and S-content in the NMOS-III NCs introduces additional recombination centers (e.g., NiS).

The photocatalytic degradation followed a two-stage first-order kinetic model, with a rapid initial phase (0–5 min) and a slower subsequent phase (5–90 min). The corresponding rate constants are presented in **Figure S5B** and **Table S5**. Both first- and second-order fitting to the kinetic models were evaluated to elucidate the best fit to the experimental performance (**Figures S5B-C** and **Table S5**). We found that the difference was marginal, and adopted the first-order model for consistency and to facilitate direct comparison with most literature reports. The rapid adsorption of dye molecules promotes the faster dye degradation within the first 5 minutes onto the active sites of the NCs. For NMOS-I and NMOS-II NCs, this process is much more efficient and fast, with NMOS-I NCs exhibiting the fastest kinetic rate of 0.289 min^{-1}. The process proceeds more rapidly because $\cdot OH^-$ radicals are generated alongside adsorption, which promotes dye molecule degradation and thereby regenerates the active sites on the surface of the NCs. This observation is supported by the EPR analysis, where only the NMOS-I and NMOS-II NCs were shown to exhibit radical formation. In the following degradation phase, for the pristine NiO and NMOS-III, this process is extremely slow, with kinetics rates of 0.002 and 003 min^{-1}, respectively. This slow degradation occurs mainly due to slow equilibrium adsorption. Conversely, for the NMOS-I and NMOS-II, this process is faster, 0.004 and 0.005 min^{-1}, respectively. Here again, due to the higher Mo-content, there is a synergistic effect between the adsorption process and radical-promoted photocatalysis.

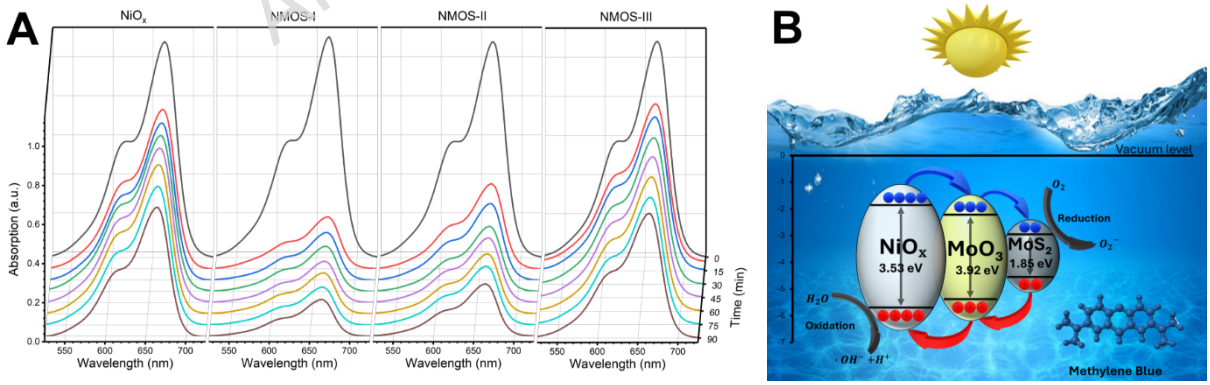

Figure 7: (A) 3D UV-visible spectra of MB photodegradation after different light irradiation times using NiO_x and NMOS-I-III NCs in aqueous solutions. Note: spectra are shown with an offset for clarity. (B) Schematic mechanism of methylene blue degradation by NMOS NCs.

The photodegradation processes involving NMOS-I-II NCs and their interaction with dyes are detailed in **Equations 1-4** and schematically illustrated in **Figure 7B**. Under illumination with visible light, photons with energy greater than or equal to the band gap of the semiconductor components (NiO_x, MoO_3, or MoS_2) excite electrons from the valence band (VB) to the conduction band (CB), generating electron-hole pairs. The photogenerated electrons and holes react with

adsorbed species (oxygen, water, or hydroxide ions) to produce reactive oxygen species, such as $\cdot O_2^-$ and $\cdot OH^-$, which are responsible for dye degradation. The $\cdot OH^-$reacts with the adsorbed MB, breaking their chromophores and leading to mineralization.[118] The schematic mechanism of methylene blue degradation by NMOS NCs.

Equation 1: NiO_X -x1 - 2MoO_3 - MoS_2 +hv→NNiO_X -x1 - 2MoO_3 - $MoS_2\left(e_{CB}^- + h_{VB}^+\right)$

Equation 2: NiO_X -x1 - 2MoO_3 - $MoS_2\left(h_{VB}^+\right)$ + H_2O→NiO@1 - 2L - MoS_2 + • OH^- + H^+

Equation 3: NiO_X -x1 - 2MoO_3 - $MoS_2\left(h_{VB}^+\right)$ + • OH^-→NiO@1 - 2L - MoS_2 + • OH

Equation 4: NiO_X -x1 - 2MoO_3 - $MoS_2(e_{CB}^-)$ + O_2→NiO@1 - 2L - MoS_2 + • O_2^-

3. Conclusions

The NMOS NCs were synthesized via a novel approach, involving the sol-gel synthesis of non-stoichiometric NiO_x NPs, followed by annealing with various molar ratios of Mo precursor, which enabled tunable multiphase compositions. Comprehensive characterization through XRD, TEM, XPS, and Raman confirmed the formation of multiphase NCs, containing non-stoichiometric NiO_x, while the MoO_3 and MoS_2 fractions increase with Mo-precursor, and that NMOS-III additionally contains NiS formed by interaction between NiO_x and MoS_4^{2-}. Optical measurements (Absorbance and PL) discovered that increasing the Mo-precursor concentration induces a shift in the absorption edge from the UV to the visible region, with band gaps decreasing from 3.66 eV (NMOS-I) to 2.93 eV (NMOS-III), due to the higher MoS_2 and NiS content.

Under visible-light irradiation, NMOS-I exhibited the highest photocatalytic activity for MB degradation (82% in 90 min), which is attributed to an optimum balance of NiO_x and MoO_3–MoS_2 phases that promote efficient p–n junction formation, thereby enhancing charge separation and minimizing electron–hole recombination. In contrast, NMOS-III demonstrated lower activity (42%), likely due to recombination centers associated with NiS and excess MoS_2. EPR measurements confirmed that $\cdot OH^-$ radicals generated by NMOS-I and NMOS-II drive the degradation process. Kinetic analysis revealed that MB degradation in NMOS-I and NMOS-II proceeds via dual stages: a rapid initial stage dominated by dye adsorption and degradation by $\cdot OH^-$ radicals, after that a slower stage controlled by slow equilibrium adsorption. NMOS-I showed the fastest overall kinetics due to efficient interaction between adsorption and photocatalysis, while higher Mo loadings (NMOS-III) reduced this effect.

In conclusion, the innovative synthesis and multi-technique characterization of this study demonstrate that NMOS NCs, particularly NMOS-I and NMOS-II, offer a promising platform for visible-light-driven photocatalysis. The novel tunable phase compositions improve charge separation and optical properties, while detailed kinetic modeling of adsorption-photocatalysis interplay provides actionable insights for designing heterostructured NCs. These findings suggest potential applications in environmental remediation, such as dye degradation, and pave the way for further optimization of heterostructured nanomaterials for advanced photocatalytic systems.

4. Methods

4.1. Experimental

4.1.1. Sol-gel synthesis of NiO_x NPs:

3.635 g of nickel(II) nitrate hexahydrate ($Ni(NO_3)_2 6H_2O$, Merck, 97%) dissolved in 5 mL of distilled water (DI water). Meanwhile, 2 g of sodium hydroxide (NaOH, Bio-Lab, 97%) was dissolved in 5 mL of DI water. Then, 0.9 mL of NaOH solution was added dropwise to the Ni solution. The resulting

light green mixture was centrifuged at 5000 RPM for 5 minutes. The precipitation was washed 3 times with DI water and dried in a vacuum oven at 80 ˚C for 1h. The obtained green powder was annealed at 270 °C for 2 h under a nitrogen atmosphere to yield dark-black powder.

4.1.2. Synthesis of NMOS NCs:

The dark-black NiO_x NPs powder was divided into four vials (with one vial serving as a reference). Three different molar ratios of ammonium tetrathiomolybdate ($(NH_4)_2MoS_4$) were added to each vial to control the relative MoO_3–MoS_2 content (labeled as I, II, and III). The molar ratios were as follows:

- NMOS-I: 0.276 mol
- NMOS-II: 0.552 mol
- NMOS-III: 0.828 mol

15 mL of DI water was added to each vial, and the mixtures were sonicated for 5 minutes. All solutions were then mixed overnight in an oil bath at 55 °C. To finalize the coating of NiO NPs with the MoS_2 layer, each sample was centrifuged at 11,000 RPM for 20 minutes. Subsequently, each sample was sonicated for 5 minutes in 3 mL of ethanol and transferred to ampoules. The ampoules were dried in a vacuum oven at 80 °C for 1 hour. Finally, the ampoules were vacuum-sealed and placed in a horizontal oven with two heat zones (350 °C and 520 °C) for 15 minutes.

4.2. Characterization Techniques

4.2.1. X-ray diffraction (XRD):

XRD patterns of the NiO_x NPs and NMOS-I-III NCs were collected in a step−scan mode at room temperature using Rigaku SmartLab SE diffractometer with 40 kV X-ray generator (Cu Kα radiation, 10−50° 2θ range, step width 0.03°). The XRD data were analyzed using MDI Jade 8.8 software, and the relative fractions of the NiO, $NaNO_3$, MoS_3, and MoO_3 phases were determined by the Reference Intensity Ratio (RIR) method.

4.2.2. High-resolution Transmission Electron Microscopy (HR-TEM):

HR-TEM analysis of the NiO_x NPs and NMOS-I-III NCs was performed using a Talos F200X S/TEM microscope (Thermo Fisher Scientific, USA) with an accelerating voltage of 200kV and an X-FEG Electron source. An energy-dispersive X-ray spectroscopy (EDS) detector (super-X EDS system) was attached to the TEM instrument, which allowed the chemical composition of the nanocrystals to be determined. The samples were prepared by dropping 5 µL of a highly diluted sample solution in ethanol onto a copper grid covered by formvar carbon.

4.2.3. X-ray photoelectron spectroscopy (XPS):

XPS spectra of the NiO_x NPs and NMOS-I-III NCs were collected using a Thermo Scientific ESCALAB QXi. The samples were irradiated with monochromatic Al Kα radiation with a spot size of 400µm. The survey scans were collected at a pass energy of 200 eV and an energy step size of 1.0 eV. High-resolution scans were collected at a pass energy of 40 eV and an energy step size of 0.1 eV. A dual-beam neutralization was used to manage charge effects. All data was processed and analyzed using Avantage software version 6.4.

4.2.4. Raman measurements

Raman analysis of NiO_x NPs and NMOS-I-III NCs was collected using a LabRAM HR Evolution system (Horiba, France) equipped with a 532 laser to minimize fluorescence interference. Spectra were acquired using an 800 mm spectrograph, which offers high sensitivity, high spectral resolution, and low stray light. A 600 gr/mm grating was employed, yielding a spectral resolution of less than 1.0 cm^{-1} per pixel. Imaging and spectral acquisition were conducted using a BXFM Olympus

modular optical microscope with a PlanFL N ×100 objective lens (NA 0.9). Each spectrum was collected with an exposure time of 0.25–0.5 seconds, averaged over 10 accumulations.

4.2.5. UV-Vis Spectrophotometer:

The absorbance spectra of the NiO_x NPs and NMOS-I-III NCs solutions were recorded in the range of 250-800 nm using a V-750 UV-visible spectrophotometer (Jasco, Japan) equipped with 60 mm integrating spheres.

4.2.6. Spectrofluorometer:

The photoluminescence (PL) spectra of the NiO_x NPs and NMOS-I-III NCs were recorded using FP-8350 Spectrofluorometer (Jasco, Japan). Here, lasers with a 250 and 532 nm wavelength were used for excitation, and the PL was measured in the range of 300-800 and 600-800 nm using an FP-8350 Spectrofluorometer (Jasco, Japan).

4.2.7. Electron Paramagnetic Resonance (EPR):

Spectra of the NiO_x NPs and NMOS-I-III NCs were recorded on a Bruker ELEXSYS 500 X-band spectrometer equipped with a Bruker ER4119HS resonator operating at a microwave frequency of 9.5 GHz. The experimental conditions for the EPR spectra were as follows: microwave power of 20 mW, 1 Gauss modulation amplitude, and a modulation frequency of 100 kHz. The sweep range was 200 Gauss, and the spectra consisted of 400 data points. The data was plotted using Origin software. 5 mg of each sample was dispersed in DI water. Each sample (200 µl) was inserted into a flat cell Suprasil for aqueous solutions (WG-808-Q, Wilmad) at room temperature. A stock solution was prepared by sonicating 25 mg of 5-tert-butoxycarbonyl-5-methyl-1-pyrroline-N-oxide (BMPO) spin trap in 5 mL DI water. Each sample consisted of a 40 µL dispersed solution with NiO and NMOS-I-III NCs in DI water (5 mg in 1mL), with 160 µL BMPO stock solution.

4.2.8. Photocatalysis

Dye degradation was performed to study the photocatalytic activity of the NiO_x NPs and NMOS-I-III NCs. A stock solution was prepared by dispersing 5 mg of methylene blue (MB) dye in 10 mL of DI water. 10 mg of each NPs sample (the NiO and NMOS-I-III NCs) was dispersed in 29 mL of DI water. For each sample, 1 mL of MO stock solution was added to 29 mL of DI water of the NiO and NMOS-I-III NCs. Each sample was placed in front of a solar simulator (model 10500, 1 sun, Abet-technologies, USA) at a distance of 10 cm. 2.5 mL of the sample was collected every 10 minutes and centrifuged at 11000 rpm for 1 minute before measuring the absorption spectrum. The degradation rate (D%) was calculated using **Equation 5** and **Equation 6**, where, C_0 and C_t is the dye concentration at $t = 0$ min (initial concentration) and $t = t$ min, respectively.

Equation 5: $$D\% = \left(1 - \frac{C_t}{C_0}\right) x100\%$$

The first-order kinetic equation is given by:

Equation 6: $$\ln\left(\frac{C_t}{C_0}\right) = k_1 t$$

Here, k_1 (min^{-1}) represents the reaction first-order rate constant derived from the slope of the $\ln\left(\frac{C_t}{C_0}\right)$ versus time (t) plot.

5. References

1. Saeed, M., Muneer, M., Haq, A. ul & Akram, N. Photocatalysis: an effective tool for photodegradation of dyes—a review. *Environ. Sci. Pollut. Res.* **29,** 293–311 (2022).

2. Prasad, N., Shalom, H., Leybovich, A., Prilusky, J. & Lena Yadgarov, L. Optimized Growth and Manipulation of Light-Matter Interaction in Stabilized Halide Perovskite Nanowire Array. at https://doi.org/10.26434/chemrxiv-2024-wk6lq-v2 (2024)

3. Joshi, N. C., Gururani, P. & Gairola, S. P. Metal oxide nanoparticles and their nanocomposite-based materials as photocatalysts in the degradation of dyes. *Biointerface Res. Appl. Chem.* **12,** 6557–6579 (2022).

4. Feng, H. peng *et al.* Core-shell nanomaterials: Applications in energy storage and conversion. *Adv. Colloid Interface Sci.* **267,** 26–46 (2019).

5. Shafiee, A. *et al.* Core–Shell Nanophotocatalysts: Review of Materials and Applications. *ACS Appl. Nano Mater.* **5,** 55–86 (2022).

6. Ogungbesan, S. O. *et al.* Transition metal oxide nanohybrid materials: A review of their structures, properties, and applications. *J. Mol. Struct.* **1337,** 142209 (2025).

7. Li, X. *et al.* Recent Progress in Metal Oxide-Based Photocatalysts for CO2 Reduction to Solar Fuels : A Review. (2023).

8. Kamo, A., Sonmezoglu, O. A. & Sonmezoglu, S. Unraveling the Effects of Strain-Induced Defect Engineering on the Visible-Light-Driven Photodynamic Performance of Zn 2 SnO 4 Nanoparticles Modified by Larger Barium Cations. (2024). doi:https://doi.org/10.1021/acsabm.4c01447

9. Kamo, A., Sonmezoglu, O. A. & Sonmezoglu, S. Ternary zinc–tin-oxide nanoparticles modified by magnesium ions as a visible-light-active photocatalyst with highly strong antibacterial activity. *Nanoscale Adv.* 6008–6018 (2024). doi:https://doi.org/10.1039/D4NA00811A

10. Kamo, A., Ozcan, A., Sonmezoglu, O. A. & Sonmezoglu, S. 10 Understanding antibacterial disinfection mechanisms of oxide-based photocatalytic materials.

11. Zaki, R. S. R. M., Jusoh, R., Chanakaewsomboon, I. & Setiabudi, H. D. Materials Today : Proceedings Recent advances in metal oxide photocatalysts for photocatalytic degradation of organic pollutants : A review on photocatalysts modification strategies. *Mater. Today Proc.* **107,** 59–67 (2024).

12. Prasad, N. *et al.* Highly Efficient Carbon-Encapsulated ZnO Nanoparticles with Enhanced Light-Matter Interactions for Photocatalytic Applications. at https://doi.org/10.26434/chemrxiv-2025-knx2z (2025)

13. Fasaki, I., Koutoulaki, A., Kompitsas, M. & Charitidis, C. Structural, electrical and mechanical properties of NiO thin films grown by pulsed laser deposition. *Appl. Surf. Sci.* **257,** 429–433 (2010).

14. Wruck, D. A. & Rubin, M. Structure and Electronic Properties of Electrochromic NiO Films. *J. Electrochem. Soc.* **140,** 1097–1104 (1993).

15. Tiwari, S. D. & Rajeev, K. P. Magnetic properties of NiO nanoparticles. *Thin Solid Films* **505,** 113–117 (2006).

16. Zheng, Z. T., Cochrane, G., Smith, G. B. & Wantenaar, G. H. J. Electrical and optical properties and structural characterisation of ITO films deposited by magnetron sputtering. *Opt. Appl.* **XLI,** 1–10 (1995).

17. Newman, R. & Chrenko, R. M. Optical Properties of Nickel Oxide. *Phys. Rev.* **114,** 1507–1513 (1959).

18. Dirksen, J. A., Duval, K. & Ring, T. A. NiO thin-film formaldehyde gas sensor. *Sensors Actuators, B Chem.* **80,** 106–115 (2001).

19. Li, F., Chen, H. Y., Wang, C. M. & Hu, K. A. A novel modified NiO cathode for molten carbonate fuel cells. *J. Electroanal. Chem.* **531,** 53–60 (2002).

20. Zhong, D., Liao, X., Liu, Y., Zhong, N. & Xu, Y. Enhanced electricity generation performance and dye wastewater degradation of microbial fuel cell by using a petaline NiO@polyaniline-carbon felt anode. *Bioresour. Technol.* **258,** 125–134 (2018).

21. Liu, L. *et al.* Activating peroxydisulfate by morphology-dependent NiO catalysts: Structural origin of different catalytic properties. *Appl. Catal. B Environ.* **256,** (2019).

22. Deraz, N. M., Selim, M. M. & Ramadan, M. Processing and properties of nanocrystalline Ni and NiO catalysts. *Mater. Chem. Phys.* **113,** 269–275 (2009).

23. Ata-ur-Rehman *et al.* Current advances and prospects in NiO-based lithium-ion battery anodes. *Sustain. Energy Technol. Assessments* **53,** 102376 (2022).

24. Varghese, B. *et al.* Fabrication of NiO nanowall electrodes for high performance lithium ion battery. *Chem. Mater.* **20,** 3360–3367 (2008).

25. Purushothaman, K. K., Manohara Babu, I., Sethuraman, B. & Muralidharan, G. Nanosheet-assembled NiO microstructures for high-performance supercapacitors. *ACS Appl. Mater. Interfaces* **5,** 10767–10773 (2013).

26. Kim, S. I., Lee, J. S., Ahn, H. J., Song, H. K. & Jang, J. H. Facile route to an efficient nio supercapacitor with a three-dimensional nanonetwork morphology. *ACS Appl. Mater. Interfaces* **5,** 1596–1603 (2013).

27. Yang, L. X. *et al.* Hydrothermal synthesis of nickel hydroxide nanostructures in mixed solvents of water and alcohol. *J. Solid State Chem.* **180,** 2095–2101 (2007).

28. Sonavane, A. C. *et al.* Efficient electrochromic nickel oxide thin films by electrodeposition. *J. Alloys Compd.* **489,** 667–673 (2010).

29. Nalage, S. R., Chougule, M. A., Sen, S., Joshi, P. B. & Patil, V. B. Sol-gel synthesis of nickel oxide thin films and their characterization. *Thin Solid Films* **520,** 4835–4840 (2012).

30. Salavati-Niasari, M., Mir, N. & Davar, F. A novel precursor in preparation and characterization of nickel oxide nanoparticles via thermal decomposition approach. *J. Alloys Compd.* **493,** 163–168 (2010).

31. Imran Din, M. & Rani, A. Recent advances in the synthesis and stabilization of nickel and nickel oxide nanoparticles: A green adeptness. *Int. J. Anal. Chem.* **2016,** (2016).

32. Hashem, M. *et al.* Fabrication and characterization of semiconductor nickel oxide (NiO) nanoparticles manufactured using a facile thermal treatment. *Results Phys.* **6,** 1024–1030 (2016).

33. Mohan, V. K. *et al.* Defect Tailored NiO Quantum Dots via Energy-Efficient Synthesis: Electronic Transport and Selective Cytotoxicity. *ACS Omega* **10,** 36697–36707 (2025).

34. Zhu, Y. *et al.* Synthesis of Large-Sized van der Waals Layered MoO_3 Single Crystals with Improved Dielectric Performance. *Precis. Chem.* **2,** 406–413 (2024).

35. Floquet, N., Bertrand, O. & Heizmann, J. J. Structural and morphological studies of the growth of MoO_3 scales during high-temperature oxidation of molybdenum. *Oxid. Met.* **37,** 253–280 (1992).

36. Yin, H. *et al.* High-surface-area plasmonic MoO_{3-x}: rational synthesis and enhanced ammonia borane dehydrogenation activity. *J. Mater. Chem. A* **5,** 8946–8953 (2017).

37. Pavoni, E. *et al.* First-Principles Calculation of MoO_2 and MoO_3 Electronic and Optical Properties Compared with Experimental Data. *Nanomaterials* **13,** 1319 (2023).

38. White, R. T., Thibau, E. S. & Lu, Z.-H. Interface Structure of MoO_3 on Organic Semiconductors. *Sci. Rep.* **6,** 21109 (2016).

39. Ali, S. & Farrukh, M. A. Effect of Calcination Temperature on the Structural, Thermodynamic, and Optical Properties of MoO_3 Nanoparticles. *J. Chinese Chem. Soc.* **65,** 276–288 (2018).

40. Sabhapathi, V. K. *et al.* Optical absorption studies in molybdenum trioxide thin films. *Phys. Status Solidi* **148,** 167–173 (1995).

41. Lou, S. N., Yap, N., Scott, J., Amal, R. & Ng, Y. H. Influence of MoO_3(110) Crystalline Plane on Its Self-Charging Photoelectrochemical Properties. *Sci. Rep.* **4,** 7428 (2014).

42. Xi, Q. *et al.* Improving the Thermal Stability of Inverted Organic Solar Cells by Mitigating the Undesired MoO_3 Diffusion toward Cathodes with a High-Ionization Potential Interface Layer. *ACS Appl. Mater. Interfaces* **17,** 15456–15467 (2025).

43. Liu, Y. *et al.* Effects of nano-MoO_3 on growth, quality and toxicity of soybean. *J. Sci. Food Agric.* **105,** 2012–2020 (2025).

44. Avani, A. V. & Anila, E. I. Recent advances of MoO_3 based materials in energy catalysis: Applications in hydrogen evolution and oxygen evolution reactions. *Int. J. Hydrogen Energy* **47,** 20475–20493 (2022).

45. da Silva Júnior, M. G. *et al.* A Brief Review of MoO_3 and MoO_3-Based Materials

and Recent Technological Applications in Gas Sensors, Lithium-Ion Batteries, Adsorption, and Photocatalysis. *Materials (Basel).* **16,** 7657 (2023).

46. Hussain, O. . & Rao, K. . Characterization of activated reactive evaporated MoO_3 thin films for gas sensor applications. *Mater. Chem. Phys.* **80,** 638–646 (2003).

47. Shakir, I., Shahid, M., Yang, H. W. & Kang, D. J. Structural and electrochemical characterization of α-MoO_3 nanorod-based electrochemical energy storage devices. *Electrochim. Acta* **56,** 376–380 (2010).

48. Borgschulte, A. *et al.* Hydrogen reduction of molybdenum oxide at room temperature. *Sci. Rep.* **7,** 40761 (2017).

49. Wang, L., Zhang, G.-H., Sun, Y.-J., Zhou, X.-W. & Chou, K.-C. Preparation of Ultrafine β-MoO_3 from Industrial Grade MoO_3 Powder by the Method of Sublimation. *J. Phys. Chem. C* **120,** 19821–19829 (2016).

50. Amba Sankar, K. N. *et al.* Renewable synthesis of MoO_3 nanosheets via low temperature phase transition for supercapacitor application. *Sci. Rep.* **14,** 20503 (2024).

51. Xu, H. *et al.* Hydrothermal synthesis of one-dimensional α-MoO_3 nanomaterials and its unique sensing mechanism for ethanol. *Arab. J. Chem.* **15,** 104083 (2022).

52. Yue, Q. *et al.* Mechanical and electronic properties of monolayer MoS_2 under elastic strain. *Phys. Lett. A* **376,** 1166–1170 (2012).

53. Li, T. & Galli, G. Electronic properties of MoS_2 nanoparticles. *J. Phys. Chem. C* **111,** 16192–16196 (2007).

54. Berntsen, N. *et al.* A Solvothermal Route to High-Surface-Area Nanostructured MoS_2. *Chem. Mater.* **15,** 4498–4502 (2003).

55. Ellis, J. K., Lucero, M. J. & Scuseria, G. E. The indirect to direct band gap transition in multilayered MoS_2 as predicted by screened hybrid density functional theory. *Appl. Phys. Lett.* **99,** (2011).

56. Tsokkou, D., Yu, X., Sivula, K. & Banerji, N. The Role of Excitons and Free Charges in the Excited-State Dynamics of Solution-Processed Few-Layer MoS_2 Nanoflakes. *J. Phys. Chem. C* **120,** 23286–23292 (2016).

57. Dungey, K. E., Curtis, M. D. & Penner-Hahn, J. E. Structural Characterization and Thermal Stability of MoS_2 Intercalation Compounds. *Chem. Mater.* **10,** 2152–2161 (1998).

58. Wang, N. *et al.* Synthesis of strongly fluorescent molybdenum disulfide nanosheets for cell-targeted labeling. *ACS Appl. Mater. Interfaces* **6,** 19888–19894 (2014).

59. Butanovs, E., Kuzmin, A., Butikova, J., Vlassov, S. & Polyakov, B. Synthesis and characterization of ZnO/ZnS/MoS_2 core-shell nanowires. *J. Cryst. Growth* **459,** 100–104 (2017).

60. Chia, X., Eng, A. Y. S., Ambrosi, A., Tan, S. M. & Pumera, M. Electrochemistry

of Nanostructured Layered Transition-Metal Dichalcogenides. *Chem. Rev.* **115,** 11941–11966 (2015).

61. Li, Y. *et al.* MoS_2 Nanoparticles Grown on Graphene: An Advanced Catalyst for the Hydrogen Evolution Reaction. *J. Am. Chem. Soc.* **133,** 7296–7299 (2011).

62. Qiao, X.-Q. *et al.* Tunable MoS_2/SnO_2P–N Heterojunctions for an Efficient Trimethylamine Gas Sensor and 4-Nitrophenol Reduction Catalyst. *ACS Sustain. Chem. Eng.* **6,** 12375–12384 (2018).

63. Yu, H. *et al.* Three-dimensional hierarchical MoS_2 nanoflake array/carbon cloth as high-performance flexible lithium-ion battery anodes. *J. Mater. Chem. A* **2,** 4551–4557 (2014).

64. Chen, Q., Li, Y., Li, Q., Jia, Y. & Qiao, X. 3D Hierarchical N, O Co–Doped MoS_2/NiO Hollow Microspheres as Reusable Catalyst for Nitrophenols Reduction. *ChemistrySelect* **4,** 9339–9347 (2019).

65. Arul, N. S. & Nithya, V. D. Molybdenum disulfide quantum dots: synthesis and applications. *RSC Adv.* **6,** 65670–65682 (2016).

66. Song, I., Park, C. & Choi, H. C. Synthesis and properties of molybdenum disulphide: From bulk to atomic layers. *RSC Adv.* **5,** 7495–7514 (2015).

67. Díez-garcía, M. I. & Gómez, R. Progress in Ternary Metal Oxides as Photocathodes for Water Splitting Cells : Optimization Strategies. **2100871,** (2022).

68. Ahmed, M. A., Mahmoud, A., Mohamed, A. A. & Adel, M. RSC Advances Interfacially engineered metal oxide nanocomposites for enhanced photocatalytic degradation of pollutants and energy applications. 15561–15603 (2025). doi:10.1039/d4ra08780a

69. Rezaei, M. M., Seyed Dorraji, M. S., Hosseini, S. F. & Rasoulifard, M. H. S-scheme heterojunction of MoO_3 nanobelts and MoS_2 nanoflowers for photocatalytic degradation. *Sci. Rep.* **15,** 10789 (2025).

70. Aghaei, F., Ghodsi, F. E. & Mazloom, J. Enhanced optical and electrochemical properties MoO_3-NiO-$NiMoO_4$ ternary nanocomposite thin films: influence of PEG and PVA additives. *Sci. Rep.* **15,** 26949 (2025).

71. Jiang, F., Choy, W. C. H., Li, X., Zhang, D. & Cheng, J. Post-treatment-free solution-processed Non-stoichiometric NiO_x nanoparticles for efficient hole-transport layers of organic optoelectronic devices. *Adv. Mater.* **27,** 2930–2937 (2015).

72. Aiken, J. G. & Jordan, A. G. Electrical transport properties of single crystal nickel oxide. *J. Phys. Chem. Solids* **29,** 2153–2167 (1968).

73. Mahmood, T. *et al.* Comparison of different methods for the point of zero charge determination of NiO. *Ind. Eng. Chem. Res.* **50,** 10017–10023 (2011).

74. Brito, J. L., Ilija, M. & Hernández, P. Thermal and reductive decomposition of ammonium thiomolybdates. *Thermochim. Acta* **256,** 325–338 at

https://doi.org/10.1016/0040-6031(94)02178-Q (1995)

75. Kayani, Z. N., Butt, M. Z., Riaz, S. & Naseem, S. Synthesis of NiO nanoparticles by sol-gel technique. *Mater. Sci. Pol.* **36,** 547–552 (2018).

76. Frank, A. *et al.* Structural and chemical characterization of MoO_2/MoS_2 triple-hybrid materials using electron microscopy in up to three dimensions. *Nanoscale Adv.* **3,** 1067–1076 (2021).

77. Nisar, T. *et al.* Facile Spin-Coated MoS_2 Thin Films from a Single-Source Precursor for HER Activity. *ACS Appl. Energy Mater.* **8,** 9497–9505 (2025).

78. Ipsakis, D., Heracleous, E., Silvester, L., Bukur, D. B. & Lemonidou, A. A. Reduction and oxidation kinetic modeling of NiO-based oxygen transfer materials. *Chem. Eng. J.* **308,** 840–852 (2017).

79. Ningsih, S. K. W. & Khair, M. Synthesis and Characterization of Nio Nanocrystals by using Sol-Gel Method with Various Precursors. *Makara J. Sci.* **21,** (2017).

80. Bond, B. D. & Jacobs, P. W. M. The thermal decomposition of sodium nitrate. *J. Chem. Soc. A Inorganic, Phys. Theor.* 1265 (1966). doi:10.1039/j19660001265

81. Al Boukhari, J., Khalaf, A. & Awad, R. Structural and electrical investigations of pure and rare earth (Er and Pr)-doped NiO nanoparticles. *Appl. Phys. A Mater. Sci. Process.* **126,** 1–16 (2020).

82. Shidpour, R., Vosoughi, M., Maghsoudi, H. & Simchi, A. A general two-step chemical vapor deposition procedure to synthesis highly crystalline transition metal dichalcogenides: A case study of MoS_2. *Mater. Res. Bull.* **76,** 473–478 (2016).

83. Albu-Yaron, A. *et al.* MoS_2 Hybrid nanostructures: From octahedral to quasi-spherical shells within individual nanoparticles. *Angew. Chemie - Int. Ed.* **50,** 1810–1814 (2011).

84. Flynn, C. J. *et al.* Hierarchically-structured NiO nanoplatelets as mesoscale p-type photocathodes for dye-sensitized solar cells. *J. Phys. Chem. C* **118,** 14177–14184 (2014).

85. Terlemezoglu, M., Surucu, O., Isik, M., Gasanly, N. M. & Parlak, M. Temperature-dependent optical characteristics of sputtered NiO thin films. *Appl. Phys. A* **128,** 50 (2022).

86. An, N. *et al.* Magnetic phase transition and spin-phonon coupling effect of antiferromagnetic NiO flakes probed by Raman spectroscopy. *Spectrochim. Acta Part A Mol. Biomol. Spectrosc.* **330,** 125645 (2025).

87. Sunny, A. & Balasubramanian, K. Raman Spectral Probe on Size-Dependent Surface Optical Phonon Modes and Magnon Properties of NiO Nanoparticles. *J. Phys. Chem. C* **124,** 12636–12644 (2020).

88. Seguin, L., Figlarz, M., Cavagnat, R. & Lassègues, J. C. Infrared and Raman spectra of MoO_3 molybdenum trioxides and $MoO_3 \cdot xH_2O$ molybdenum

trioxide hydrates. *Spectrochim. Acta Part A Mol. Biomol. Spectrosc.* **51,** 1323–1344 (1995).

89. Sovizi, S., Tosoni, S. & Szoszkiewicz, R. MoS_2 oxidative etching caught in the act: formation of single $(MoO_3)n$ molecules. *Nanoscale Adv.* **4,** 4517–4525 (2022).

90. Cao, Y. *et al.* Phonon modes and photonic excitation transitions of MoS_2 induced by top-deposited graphene revealed by Raman spectroscopy and photoluminescence. *Appl. Phys. Lett.* **114,** (2019).

91. Bishop, D. W., Thomas, P. S. & Ray, A. S. Raman spectra of nickel(II) sulfide. *Mater. Res. Bull.* **33,** 1303–1306 (1998).

92. Sabouri, Z. *et al.* Plant-based synthesis of NiO nanoparticles using salvia macrosiphon Boiss extract and examination of their water treatment. *Rare Met.* **39,** 1134–1144 (2020).

93. Ramesh, M., Rao, M. P. C., Anandan, S. & Nagaraja, H. Adsorption and photocatalytic properties of NiO nanoparticles synthesized via a thermal decomposition process. *J. Mater. Res.* **33,** 601–610 (2018).

94. Venkatachalapathy, M., Sambathkumar, K. & Kamal, N. R. Synthesis and characterization of structural and magnetic properties of Fe doped NiO nanoparticles. *Dig. J. Nanomater. Biostructures* **19,** 451–458 (2024).

95. Dong, D. M. *et al.* Determination of nitrite using UV absorption spectra based on multiple linear regression. *Asian J. Chem.* **25,** 2273–2277 (2013).

96. Kumari, J. & Mangala, P. Fabrication and Characterization of Molybdenum Trioxide Nanoparticles and their Anticancer, Antibacterial and Antifungal Activities. *Malaysian J. Chem.* **24,** 36–53 (2022).

97. Jalilli, J. N. Comparative Optical Properties of Amorphous and Crystalline MoO_3 Films by Spectroscopic Ellipsometry Study. *Int. J. Nanosci.* **24,** 1–7 (2025).

98. Jung, D. H., So, H. S., Lee, H., Park, J.-Y. & Kim, H.-K. Optical properties of MoO_3/Ag/MoO_3 multilayer structures determined using spectroscopic ellipsometry. *J. Vac. Sci. Technol. A Vacuum, Surfaces, Film.* **37,** (2019).

99. Nagendra Babu, A. P., Pradeep, N. & Renuka, C. G. Sheet-like MoO_3 nanostructures with improved charge storage: Relationships among structural, optical, and electrochemical properties. *Next Energy* **8,** 100352 (2025).

100. Ali, L., Lee, Y. J., Kim, J. S. & Byeon, C. C. Sonication-assisted ion-intercalation exfoliation of MoS_2 quantum dots. *J. Mater. Res.* **38,** 4583–4594 (2023).

101. Salavati-Niasari, M., Davar, F. & Emadi, H. Hierarchical nanostructured nickel sulfide architectures through simple hydrothermal method in the presence of thioglycolic acid. *Chalcogenide Lett.* **7,** 647–655 (2010).

102. Baroot, A. Al *et al.* Enhancement of catalytic reduction of 4-nitrophenol using MoO_3 nanobelts incorporated SiO_2 nanocomposite fabricated by nanosecond

pulsed laser ablation technique. *Phys. Scr.* **98,** (2023).

103. Duan, W. J., Lu, S. H., Wu, Z. L. & Wang, Y. S. Size effects on properties of NiO nanoparticles grown in alkalisalts. *J. Phys. Chem. C* **116,** 26043–26051 (2012).

104. Kumari, L., Li, W. Z., Vannoy, C. H., Leblanc, R. M. & Wang, D. Z. Vertically aligned and interconnected nickel oxide nanowalls fabricated by hydrothermal route. *Cryst. Res. Technol.* **44,** 495–499 (2009).

105. Gandhi, A. C. & Wu, S. Y. Strong Deep-Level-Emission Photoluminescence in NiO Nanoparticles. *Nanomaterials* **7,** 18–20 (2017).

106. Koike, K., Goto, T., Nakamura, S., Wada, S. & Fujii, K. Investigation of carrier transfer mechanism of NiO-loaded n-type GaN photoanodic reaction for water oxidation by comparison between band model and optical measurements. *MRS Commun.* **8,** 480–486 (2018).

107. Basavalingaiah, K. R. NiO and Ag@NiO Nanomaterials for Enhanced Photocatalytic and Photoluminescence Studies: Green Synthesis Using Lycopodium Linn. *Asian J. Eng. Appl. Technol.* **8,** 79–85 (2019).

108. Wen, Y. Y. *et al.* Synthesis of Monolayer MoS_2 by CVD Approach. 1034–1039 (2016). doi:10.2991/ame-16.2016.167

109. Tonndorf, P. *et al.* Photoluminescence emission and Raman response of monolayer MoS_2, $MoSe_2$, and WSe_2. *Opt. Express* **21,** 4908 (2013).

110. Shalom, H., HaShachar Wallach, A., Carmieli, R. & Yadgarov, L. Europium doping effects on the properties of $CsPbBr_3$ nanocrystals: in situ vs. ex situ synthetic path analysis. *Nanoscale* **17,** 20420–20434 (2025).

111. Zang, L. Y. & Misra, H. P. EPR kinetic studies of superoxide radicals generated during the autoxidation of 1-methyl-4-phenyl-2,3-dihydropyridinium, a bioactivated intermediate of Parkinsonian-inducing neurotoxin 1-methyl-4-phenyl-1,2,3,6-tetrahydropyridine. *J. Biol. Chem.* **267,** 23601–23608 (1992).

112. Zhao, H., Joseph, J., Zhang, H., Karoui, H. & Kalyanaraman, B. Synthesis and biochemical applications of a solid cyclic nitrone spin trap: A relatively superior trap for detecting superoxide anions and glutathiyl radicals. *Free Radic. Biol. Med.* **31,** 599–606 (2001).

113. Rosenblum, W. I. & El-Sabban, F. Dimethyl sulfoxide (dmso) and glycerol, hydroxyl radical scavengers, impair platelet aggregation within and eliminate the accompanying vasodilation of, injured mouse pial arterioles. *Stroke* **13,** 35–39 (1982).

114. Sedova, A. *et al.* Exploring Halide Perovskite Nanocrystal Decomposition: Insight by In-Situ Electron Paramagnetic Resonance Spectroscopy. 1–29 at https://doi.org/10.26434/chemrxiv-2024-73fhj (2024)

115. Nosaka, Y. & Nosaka, A. Understanding Hydroxyl Radical ($\cdot OH^-$) Generation Processes in Photocatalysis. *ACS Energy Lett.* **1,** 356–359 (2016).

116. Tichapondwa, S. M., Newman, J. P. & Kubheka, O. Effect of TiO_2 phase on the photocatalytic degradation of methylene blue dye. *Phys. Chem. Earth* **118–119,** 102900 (2020).

117. Siddeeg, S. M., Tahoon, M. A., Mnif, W. & Ben Rebah, F. Iron Oxide / Chitosan Magnetic Nanocomposite Immobilized Manganese Peroxidase for. *Processes* **8,** 1–12 (2020).

118. Noua, A. E. *et al.* Methylene blue degradation with Pt-enhanced Ni/NiO nanocomposites: Adsorption, photocatalytic and magnetic insights. *Inorg. Chem. Commun.* **177,** 114388 (2025).

Author contributions statement

H.S. conceptualized the experiment(s), developed methodology, conducted investigation, curated data, performed analysis, wrote the manuscript, and contributed to writing – review & editing. S.T. assisted with synthesizing and measuring absorbance, photoluminescence, and dye degradation. O.B. performed TEM experiments. I.P. conducted Raman spectroscopy. R.C. conducted EPR experiments. L.Y. supervised, handled project administration, and contributed to writing, review & editing. All authors reviewed the manuscript.

Data availability

The data supporting the conclusions of this paper are available within the manuscript and its supplementary information.

Acknowledgements

We sincerely thank Pini Shekhter from the Center for Nanoscience and Nanotechnology, Tel Aviv University, Ramat Aviv, Tel Aviv 6997801, Israel, for his invaluable assistance with the XPS measurements. We also express our sincere gratitude to Iddo Pinkas from the Department of Chemical Research Support at the Weizmann Institute of Science for his invaluable assistance with the Raman measurements. His expertise was instrumental in the analysis presented in this work. We also extend our deep appreciation to all colleagues whose contributions were essential to the success of this research. Their time, expertise, and collaborative efforts were greatly valued.

Funding:

This research was funded by the Israel Ministry of Energy and the Israel Ministry of Innovation, Science, and Technology.